POLITECNICO DI TORINO

MASTER's Degree in MECHATRONIC ENGINEERING



MASTER's Degree Thesis

Dynamic Beam Shaping Architecture for High-Energy Lasers

Supervisors Candidate

Prof. Guido PERRONE Maria NICASSIO

Ing. Sabina ZAIMOVIC

Ing. Valentina SERAFINI

OCTOBER 2025

Dynamic Beam Shaping Architecture for High-Energy Lasers

Maria Nicassio

Abstract

Dynamic beam shaping has recently emerged as a new frontier in high-power laser systems for advanced industrial material processing. Through the inclusion of adaptive optics elements, the spatial intensity profile of laser beams becomes a new parameter to improve in real-time the thermal and mechanical interactions with the workpiece. A wide range of applications require high-power or high-energy lasers: the technology employed in cutting, welding, surface treatment, and additive manufacturing sees a continuous evolution in terms of process efficiency, quality, and versatility. However, the potential of static beam shaping methods is strongly limited by the susceptibility to light intensity variation of the input laser beam and real-time process phenomena.

In this context, deformable mirrors (DMs) present a promising solution to actively tailor wavefronts and correct aberrations at high-spatial frequency. Despite their proven effectiveness in fields such as astronomy, microscopy, and biomedical imaging, the integration of DMs into high-power laser optical chains is not straightforward. Key difficulties include managing thermal loads, achieving the desired intensity shape, and implementing a robust, real-time control aligned to the stringent industrial requirements. This thesis focuses on the design and implementation of a basic optical chain incorporating a deformable mirror for dynamic beam shaping in high-energy laser systems. The primary objective is to develop an adaptive optics-based solution capable of real-time modulation of beam profiles, enabling tailored energy distribution to optimize laser-material interactions. The research combines theoretical optical design, numerical simulations, and experimental validation to address the complexities of DM integration.

Optical simulations based on geometric optics and physical optics propagation are employed to optimize the optical chain, ensuring minimal aberrations on the source beam and efficient modulation at the focus. The deformable mirror's behaviour is modelled in Zemax OpticStudio and through Python packages as a continuous phase plate, which add aberrations defined as a linear combination of Zernike polynomials. An experimental test bench is constructed to evaluate the DM's dynamic response and beam shaping capabilities in practical scenarios. The influence of low and high order modes, such as defocus, astigmatism, coma, quadrifoil, pentafoil and spherical aberrations, is evaluated to obtain common intensity profiles (top-hat, ellipse, dough-nut).

Results demonstrate that the introduction of a DM enables significant enhance-

ments in beam shaping flexibility, allowing quick adjustments of beam profiles, tailored to specific industrial processing needs. The real-time feedback, realized by a CMOS wavefront sensor, enables the active driving of the mirror in a zonal or in a modal way. This method is a starting point for the development of smarter laser manufacturing systems capable of higher precision, reduced processing times, and improved material properties.

In conclusion, the designed dynamic beam shaping system represents an intriguing possibility in high-energy laser technology with significant implications for industrial material processing. By harnessing the potential of deformable mirrors within an optimized optical chain, this work aims to improve the efficiency and versatility of the optical chain, supporting the goals of Industry 4.0 and beyond.

ACKNOWLEDGMENTS

to G.N, for all your love.

Table of Contents

1	Sta	te of art and Theoretical Background	1				
	1.1	Overview of Adaptive Optics					
	1.2	Beam Intensity Shaping					
	1.3	Theoretical Background	5				
		1.3.1 WFE and Phase modulation	7				
		1.3.2 Zernike polynomials	8				
2	Deformable Mirror (DM) Design and Control						
	2.1	Mechanical Structure and Properties of DMs	12				
	2.2	Compensation Techniques	16				
		2.2.1 Zonal compensation	19				
		2.2.2 Modal compensation	20				
	2.3	Selected DM Hardware	22				
3	Opt	tical System Simulation	25				
	3.1	Optical Chain Design	25				
	3.2	Python Simulation	27				
	3.3	Zemax Implementation	32				
4	Exp	perimental Implementation and Results	36				
	4.1	Laboratory Optical Setup	37				
	4.2	Results	38				
5 Conclusions and Future Work							
Bi	bliog	graphy	40				
D	edica	ations	47				

List of Figures

1.1	Example of aspheric lens group shaping by Gao et al. [18]	4
1.2	Example of microlens array shaping by [19]	4
1.3	Example of DOEs shaping by [20]	5
1.4	Typical light rays in (a) propagation, (b) reflection, and (c) refraction.	5
1.5	Profiles of the electric and magnetic fields in a light wave at an instant	
	of time	6
1.6	Chief ray, Marginal ray and intermediate images and planes definition	
	in geometrical optics	7
1.7	Wavefront representation in geometrical and wave optics [21]	8
1.8	Example of reflection by [23] with a non-aberrated wavefront incident	
	on a flat mirror surface (a), an aberrated front on a flat mirror surface	
	(b) and of a wavefront correction using a DM with an appropriate	
	conjugate surface profile (c).	8
1.9	Working principle of a LCPM as illustrated by [24]	8
1.10	First 15 Zernike modes as phase added by 1 wave of aberration	11
2.1	Mechanical characterization of DMs	13
2.2	Example of Hex Tip-Tilt-Piston Deformable Mirror by [26]	13
2.3	Actuators underlying mechanisms	14
2.4	Continuous surface DMs: (a) discrete position actuators, (b) discrete	
	force actuators, (c) bending moment actuators, (d) monolithic mirror	
	[29]	15
2.5	Structure of an edge actuated DM [29]	15
2.6	17-channel MMDM from [30]	16
2.7	Examples of unimorph and bimorph DMs	17
2.8	Indirect method of maximizing intensity	18
2.9	Example of negative feedback control scheme for AO	18
2.10	Possible paths of WFE control using AO	19
2.11	Correcting wavefront fitting with an OKO MMDM	21
2.12	Correcting wavefront fitting with an OKO membrane mirror	22
2.13	DM3217 piezoelectric bimorph deformable mirror from [45]	22
2.14	Shack-Hartmann wavefront sensor supplied by [45]	23
2.15	Results of the DM3217 calibration at $AoI = 0^{\circ}$	24
2.16	Brass alignment mask for correct centering at $AoI = 45^{\circ}$	24

LIST OF FIGURES

3.1	Lens group designed in Zemax OpticStudio for a more accurate beam	
	expansion	26
3.2	Single lens configuration for beam expansion	27
3.3	Sketch of the optical setup corresponding to the simulation process in	
	Beamspot Analyzer	28
3.4	Main window of the software Beamspot Analyzer including the input	
	column on the left, the focus-plane result plots in the central column	
	and a 3D view of the beamspot around the image plane on the right.	28
3.5	Beam shaping with $Z_4=0.5$ waves and $Z_6=0.5$ waves	31
3.6	Beam shaping with $Z_4=0.5$ waves and $Z_9=-0.5$ waves	31
3.7	Beam shaping with $Z_4 = 0.5$ waves and $Z_{11} = 0.5$ waves	31
3.8	Zemax model of the optical chain reported in Table 3.2	32
3.9	Total irradiance at focus from Zemax simulation	34
3.10	Wavefront error after $Z_4=0.5$ waves and $Z_6=0.5$ waves	35
3.11	Wavefront error after $Z_4=0.5$ waves and $Z_9=-0.5$ waves	35
3.12	Wavefront error after $Z_4 = 0.5$ waves and $Z_{11} = 0.5$ waves	35
4 1		27
4.1	Scheme of the laboratory optical setup	37
4.2	Laboratory setup for the DM testing	37
43	Photon Loop window of a calibration process	38

List of Tables

1.1	Desired intensity profiles after beam shaping	3
1.2	First 15 Zernike modes	10
2.1	Test aberration for MrFit	21
3.1	Lens data for the collimator and beam expander configuration	26
3.2	Final design of the implemented optical chain	27
4.1	Components of the laboratory setup	38

Acronyms

DM Deformable mirror.

AO Adaptive Optics.

DBS Dynamic Beam Shaping.

AM Additive Manufacturing.

LPBF Laser Power Bed Fusion.

DED Direct Energy Deposition.DOE Diffractive Optical Element.

MEMS Micro Electro Mechanical Systems.

EP Entrance Pupil.

PSF Point Spread Function.

FFT Fast Fourier Transform.

WFE Wave Front Error.

OPD Optical Path Difference.

LCPM Liquid Crystal Phase Modulator.

RMS Root Mean Square.

PMN Lead-Magnesium-Niobate.PZT Lead-Zirconite-Titanite.

MMDM Micro-machined Membrane Deformable Mirror.

WFS Wave Front Sensor.

SHWS Shack-Hartmann Wavefront Sensor.

CCD Charged-Couple Device.

CA Clear Aperture.

AoI Angle of Incidence.

SMF Single-Mode Fibers.

MMF Multiple-Mode Fibers.

NA Numerical Aperture.

EFL Effective Focal Length.

BFL Back Focal Length.

POP Physical Optical Propagation.

GUI Graphical User Interface.

Chapter 1

State of art and Theoretical Background

1.1 Overview of Adaptive Optics

Adaptive optics (AO) is a rapidly developing branch of applied optics, aimed to the active compensation of phase aberrations far more complex than focus: it deals with the control of light in a *real-time* and mostly *closed-loop* fashion.

Therefore, adaptive optics is a subset of a much broader discipline, active optics. The literature often confuses and interchanges the usage of these terms. A widely used practice in the astronomy community, for example, is to differentiate them by bandwidth: Wilson et al. [1] refer to systems operating below 0.1 Hz as active and those operating above 0.1 Hz as adaptive.

The potential of adaptive optics is being utilized in a wide range of fields, each presenting its own distinct challenges and requirements. For example, it is widely applied in astronomical imaging systems [2], biomedical and retinal imaging [3], microscopy [4], metrology [5], beam propagation systems [6], laser manufacturing and processing [7], and free-space laser communications systems [8]. In particular, AO is one of the technical solution for Dynamic Beam Shaping (DBS) in metal laser Additive Manufacturing (AM): the modulation of the energy distribution of the laser beam significantly impacts the quality of printed parts. Although the Gaussian beam is widely employed, it has serious drawbacks in the AM process, such as unstable printing quality, low energy utilization, and narrow process [see 7]. The uneven energy distribution results in power spattering and porosity. Instead, the top-hat beam has a uniform laser energy distribution on the working surface, which dramatically reduces the thermal gradient inside the melt pool, resulting in a more stable weld zone and an higher efficiency of laser printing. Other energy distribution can also be of interest, when compared to a Gaussian beam, such as the doughnut: this latter permits to obtain parts with higher density and equiaxed crystals, but the resulting shallower melt pool reduce the connection reliability between the newly printed layer and the completed layer.

The use of AO has been limited by the technology available and its development has been accelerated in the past forty years by a better understanding of physical optics and the methods for controlling light, along with the technological development of new materials and control electronics.

Although the scientific and industrial use of AO has only recently emerged due to greater awareness, humans have actually already come into contact with this technology: for example, the animal visual system is itself a form of adaptive optics being in use for much longer than recorded history. The eye-brain combination is capable of adapting to various external conditions (defocus, tilt, intensity variations) applying a correction through biomechanical movement of the lens, the cornea or the iris.

From an historical point of view, Archimedes' heat ray is cited as an early use of AO. This defensive solution is one of the weapons devised by the prominent inventor to counter the Roman siege to the Kingdom of Syracuse by sea and land in 213 BC at the height of the Second Punic War (218–201 BC). According to posthumous historical accounts [9], Archimedes may have been used polished oblong mirrors tipped to catch the sun's rays and direct them at the approaching wooden ships. Whether this is the subject of ongoing debate, the destruction of the Roman fleet by fire has permeated the collective imagination.

However, AO has not been considered a possible solution until 1953 as even Isaac Newton did not include it in his treatise Opticks (1730) [10] while discussing the atmospheric turbulence limitations of astronomy.

1.2 Beam Intensity Shaping

The impact of the modulation of the distribution of laser beam energy has been widely studied in laser manufacturing: Table 1.1 reports a review of the possible desired intensity profiles and the relative process. There are many methods of beam shaping, with different degrees of complexity and practicality.

A preliminary distinction can be made between the use of refractive optics and diffractive optics. Refractive elements, in general, consist of a single bulk unit, whose shape and refractive index determine its imaging properties. According to refraction theory, light can be thought of as travelling in straight lines in a medium of constant refractive index and a change in direction happens where the refractive index changes. Diffractive elements, instead, are made of many different zones. The final image is a coherent superposition of light diffracted from the various zones. Refraction and diffraction occur simultaneously, making the final output a combination of the effects.

The presence of a feedback control and actuation distinguishes active optics from static optics. Three typical example of static methods are aspheric lens group shaping,

Table 1.1: Desired intensity profiles after beam shaping.

Beam shape	Process	Profile
Annular or Doughnut	Laser cutting [11] LPBF [7] DED [7]	- 0.0 A Account parameter
Bessel	Welding [12] LPBF [7]	- 0 a a - 0 de pumpa paginuna - 0 2
Elliptical	Welding [13] [14] LPBF [7]	- 0.8 Accounts proposed to - 0.0 - 0
Flat-top or Top-hat	LPBF [7]	- 0.8 - 0.8 - 0.0
Split spots	Hardening [15] Welding [16]	- a.a. Account putperson
Square	Hardening [15] Cladding [17]	- 0.8 A No. 2014 P. 157
Wobbled	Laser cutting [11]	- 0.8 Augusta projection - 0.2 - 0.2

microlens array shaping, and Diffractive Optical Elements (DOEs) shaping. The first one can redistribute the beam energy optimizing the Point Spread Function (see section 1.3) of the lens group in order to obtain the intensity target, as shown in Figure 1.1. This solution has high energy utilization and temperature resistance, which is more beneficial for high-power laser beam shaping, while it is more susceptible to light intensity variation of the input laser beam.

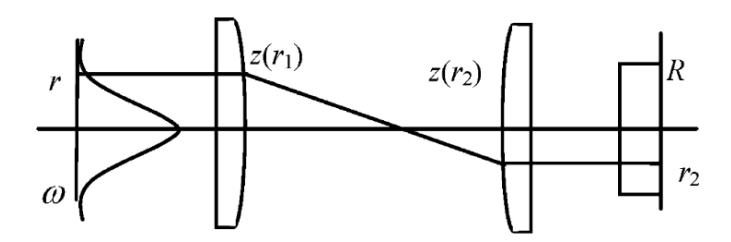


Figure 1.1: Example of aspheric lens group shaping by Gao et al. [18].

Microlens arrays (Figure 1.2), instead, divide the incoming beam into several sub-beams and focus them on the output plane: this system can be useful when the initial beam is unknown or multimode although it increases the complexity of the system and the manufacturing cost.

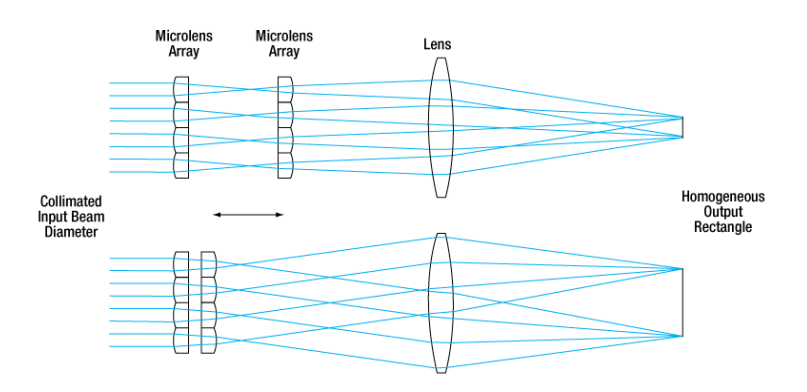


Figure 1.2: Example of microlens array shaping by [19].

DOEs (Figure 1.3) are optical elements with high diffraction efficiency, based on the theory of diffractive optics, and also used to shape beams for metal welding. They compensate the phase of the input beam in a static way, changing the transmission characteristics and the beam's intensity.

Despite the relative simplicity of the static techniques shown so far, the world of adaptive optics is shifting towards dynamic solutions such as active grating, liquid crystal spatial light modulators, MEMS high-speed segmented micromirrors, and Deformable Mirrors. These methods allow to generate multiple foci, variation in phase and focal depth, and obtain beam shaping in surface or bulk dielectrics. For example, DMs influence, as DOEs, the incoming beam's phase, although they can be

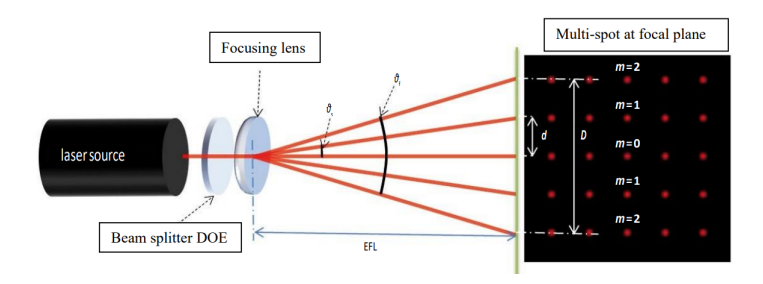


Figure 1.3: Example of DOEs shaping by [20].

inserted in a closed-loop and obtain multiple intensity profiles with the same setup and independently of the laser source. In this way, the same machine can be adapted to different industrial processes.

1.3 Theoretical Background

The subject of this thesis requires the definition of certain theoretical concepts, such as the distinction between geometrical optics and wave optics.

In the study of geometrical optics, the interaction of light waves with plane and spherical surfaces (f.e. mirrors and lenses) is represented in terms of light rays. Each ray indicates the geometrical path along which the light moves as it leaves the source. This geometrical construct helps studying the phenomena of propagation, reflection, and refraction of light and illustrating them as in Figure 1.4. An optical chain is usually composed of bulk elements mounted in a common optical medium (f.e. air or water) and the geometrical plane that separates one optical medium from another is referred to as interface. Each medium is characterized by a constant called index of refraction n, that influences the bending of the transmitted ray at interface.

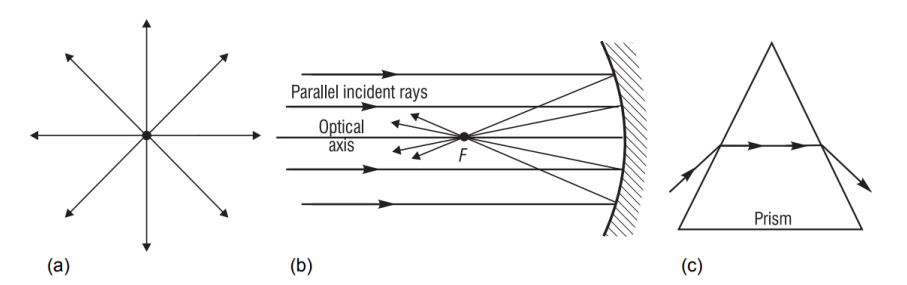


Figure 1.4: Typical light rays in (a) propagation, (b) reflection, and (c) refraction.

Conversely, the behaviour of light interacting with optical elements of similar or smaller order of magnitude of its wavelength λ , such as small objects or pinholes, can only be interpreted using wave optics (also called physical optics). In this theoretical frame, light is treated as a series of propagating electric and magnetic field oscillations. Figure 1.5 shows a profile of the transverse electric field E and magnetic field B at

one instant of time, highlighting the sinusoidal form of the varying fields. Phenomena, such as interference, diffraction, and polarization, are usually studied considering only the variation of one field (f.e. the E-field) due to the equivalence of the two solutions.

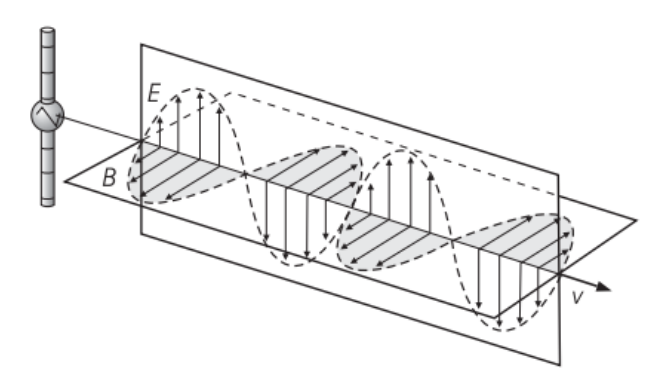


Figure 1.5: Profiles of the electric and magnetic fields in a light wave at an instant of time.

Other fundamental concepts in geometrical optics, when addressing an optical system, need to be defined. In particular, the object is the element on the left of the optical system and the apparent aperture of the imaging system as seen from its side is called the entrance pupil (EP), while the apparent aperture as as seen from the image plane, where the result of the imaging process is visible, is referred to as exit pupil (XP). The knowledge of these virtual apertures helps describing the optical chain and define certain elements, such as the marginal ray and the chief ray. Rays confined to a 2D plane (f.e the y-z plane) are called meridional rays. The marginal ray and the chief ray are two special meridional rays, illustrated in Figure 1.6, and together define the properties of the object, images, and pupils. The marginal ray starts at the axial object position, goes through the edge of the entrance pupil, and defines image locations and pupil sizes. It propagates to the edge of the stop and to the edge of the exit pupil. The *chief ray* starts at the edge of the object, goes through the center of the entrance pupil, and defines image heights and pupil locations. It goes through the center of the stop and the center of the exit pupil. When the marginal ray crosses the axis, an image is located, and the size of the image is given by the chief ray height in that plane. Whenever the chief ray crosses the axis, a pupil or the stop is located, and the pupil radius is given by the marginal ray height in that plane.

The Point Spread Function (PSF) of an optical system, instead, is the irradiance distribution that results from a single point source. It can be computed according to geometrical optics using ray tracing or according to physical optics using a Fast Fourier Transform (FFT) propagation algorithm. It gives a valid measure for the quality of an optical system, revealing the presence of diffraction or aberrations. The image formation process can be also seen as a convolution of the object and the PSF.

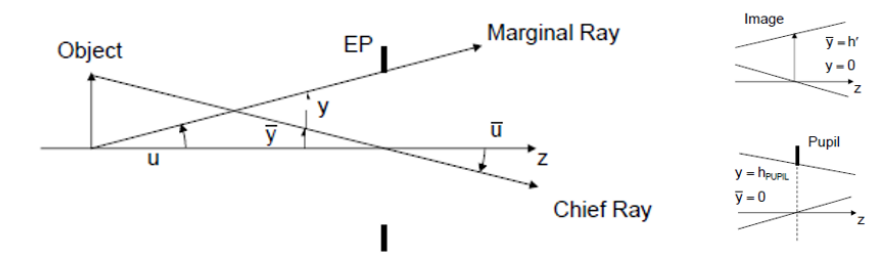


Figure 1.6: Chief ray, Marginal ray and intermediate images and planes definition in geometrical optics.

1.3.1 WFE and Phase modulation

Wavefront is a key term in adaptive optics. In terms of geometrical optics, it can be defined as a continuous surface that is orthogonal to all rays in the light beam. In wave optics, instead, the electric field phasor of a monochromatic plane wave can be represented in the form

$$\underline{\underline{E}(\underline{r})} = \underline{\underline{E}}(0) \cdot e^{-i\underline{\mathbf{k}}\cdot\underline{\mathbf{r}}} \tag{1.1}$$

where \underline{k} is the wave vector, which is perpendicular to both \underline{E} and \underline{H} vectors of the electromagnetic field and has a modulus depending on the wavelength in the medium λ as $k = \frac{2\pi}{\lambda}$; E(r) describes the electric field magnitude; $\underline{k} \cdot \underline{r}$ defines the phase term taking into account the wave propagation. Surfaces of equal phase are called wavefronts. At any given moment in time, all points on a wavefront oscillate in phase. In the special case of plane waves, the wavefronts are flat, infinite planes perpendicular to the direction of propagation. This idealization is a good approximation when the source is very far away. However, in more general and realistic situations, wavefronts can take on a variety of shapes depending on the source and the medium through which the wave propagates. For example, waves emanating from a point source in a homogeneous medium produce spherical wavefronts, where each wavefront is a sphere centered on the source. In inhomogeneous or anisotropic media, the wavefronts can become distorted, leading to more complex geometries such as ellipsoidal or irregular surfaces. Figure 1.7 provides a comparison between wavefront concepts in different optics.

In adaptive optics, the wavefront is usually the quantity to change in order to alter the propagation characteristics of the beam. It is approximated in many cases by the distribution of optical phase and can be evaluated through simulation at the intermediate pupils of the optical system. The wavefront shape can be corrected by modifying the optical phase, introducing or removing aberrations. The operation of phase modulation is based on the control of the Optical Path Difference (OPD),

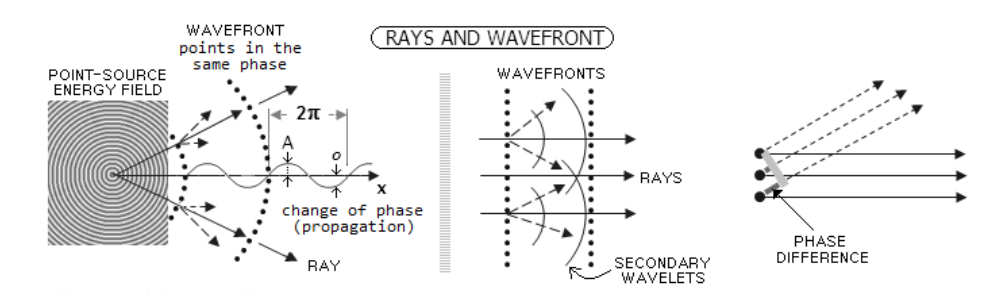


Figure 1.7: Wavefront representation in geometrical and wave optics [21].

which can be written as $OPD = n \cdot \Delta z$, where n is the refractive index, and Δz is the path travelled by the wave. It is related to the phase ϕ as $\phi = \frac{2\pi}{\lambda} \cdot OPD$. Wavefront correctors such as DMs modulate Δz , operating in the reflective mode, while others (Liquid Crystals Phase Modulators) modulate the refraction index n of the LC layer under the applied electric field in transparent or reflective mode. Figure 1.8 and Figure 1.9 illustrate the working principles of DMs and LCPMs: although the latter technology is a low-cost solution, its main drawbacks are slow response, dispersion, relatively high optical losses, pixelated response and polarization sensitivity [22].

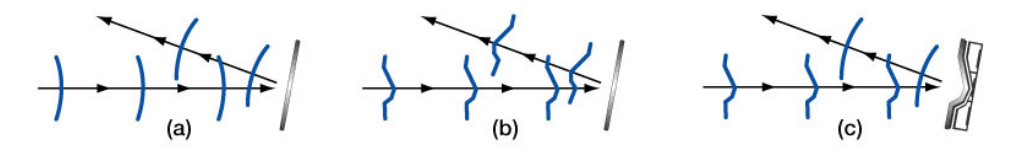


Figure 1.8: Example of reflection by [23] with a non-aberrated wavefront incident on a flat mirror surface (a), an aberrated front on a flat mirror surface (b) and of a wavefront correction using a DM with an appropriate conjugate surface profile (c).

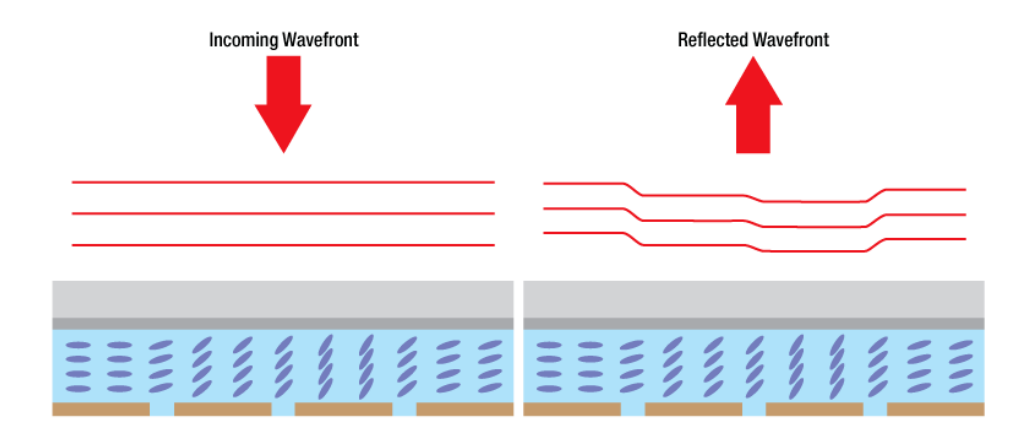


Figure 1.9: Working principle of a LCPM as illustrated by [24].

1.3.2 Zernike polynomials

Zernike polynomials were first derived by Fritz Zernike in 1934. They are useful in expressing wavefront data since they are of the same form as the types of aberrations

often observed in optical tests. In particular, the normalized Zernike expansion provides a clear and quantitative way to describe optical aberrations: each coefficient corresponds directly to the Root Mean Square (RMS) wavefront error associated with a specific aberration mode. Moreover, these coefficients are independent of the number of terms used in the expansion, thanks to the orthogonality of the polynomials. This means that additional terms can be included without altering those already determined.

Physically, a Zernike coefficient with larger magnitude indicates a greater contribution of that mode to the total RMS wavefront error, and therefore a stronger negative impact on the overall optical performance of the system. For these reasons, Zernike polynomials have become a powerful and widely used tool in adaptive optics, where they allow precise characterization and correction of complex wavefront distortions. These polynomials are a complete set in two variables, r and θ , that are orthogonal in a continuous fashion over the unit circle. The treatment of the calculations in polar coordinates and the orthonormality of this polynomial series justify the description of a WFE added by an AO element as a combination of Zernike terms.

There are multiple conventions adopted in the scientific literature, which mainly differ by order, normalization factors, and nomenclature: this thesis will refer to the Noll [25] description, as it is often the mathematical base in Python packages and simulation software as Zemax OpticStudio.

The polynomials are a product of angular functions and radial polynomials (developed from the Jacobi ones) and defined as:

$$Z_{\text{even j}} = \sqrt{n+1} R_{\text{n}}^{\text{m}}(r) \sqrt{2} \cos m\theta$$

$$Z_{\text{odd j}} = \sqrt{n+1} R_{\text{n}}^{\text{m}}(r) \sqrt{2} \sin m\theta$$

$$m \neq 0$$
(1.2)

$$Z_{\rm j} = \sqrt{n+1} \, R_{\rm n}^0(r)$$
 $m = 0$ (1.3)

where n is the radial degree, m the azimuthal frequency of the polynomial Z_n^m , j is a mode ordering number function of n and m and

$$R_{\rm n}^{\rm m}(r) = \sum_{s=0}^{(n-m)/2} \frac{(-1)^{\rm s} (n-s)!}{s! \left[(n+m)/2 - s \right]! \left[(n-m)/2 - s \right]!} r^{\rm n-2s}$$
 (1.4)

The RMS standard deviation from a non-aberrated wavefront is given by:

$$RMS = \begin{cases} \sqrt{2}\sqrt{n+1} & \text{if} \quad m \neq 0\\ \sqrt{n+1} & \text{if} \quad m = 0 \end{cases}$$
 (1.5)

From a mathematical point of view, the phase ϕ of a beam can be described as a linear combination of the desired N Zernike terms, as per:

$$\phi(\rho, \theta) = \sum_{j=1}^{N} A_j Z_j(\rho, \theta), \tag{1.6}$$

where A_{j} is the j-th term coefficient expressed in rad, as the phase.

This coefficient can also be calculated starting from the OPD, considering that the coefficient in OPD, $A_{\rm j,OPD}$, is related to the value in rad as $A_{\rm j} = \frac{2\pi}{\lambda} \cdot A_{\rm j,OPD}$. Alternatively, each coefficient can be expressed in number of waves $N_{\rm w}$, to take in consideration that one wave of aberration correspond to a 2π rad variation in phase, resulting in $A_{\rm j} = 2\pi \cdot A_{\rm j,w}$.

The first 15 Zernike modes in Noll [25] are illustrated in Table 1.2 and the corresponding phase after 1 wave of aberration in Figure 1.10.

Table 1.2: First 15 Zernike modes.

n	m	Noll j-order	RMS	Name
0	0	1	1	Piston
1	1	2	2	Tilt X
1	-1	3	2	Tilt Y
2	0	4	$\sqrt{3}$	Defocus
2	-2	5	$\sqrt{6}$	Astigmatism 45°
2	2	6	$\sqrt{6}$	Astigmatism 0°
3	-1	7	$\sqrt{8}$	Coma Y
3	1	8	$\sqrt{8}$	Coma X
3	-3	9	$\sqrt{8}$	Trefoil Y
3	3	10	$\sqrt{8}$	Trefoil X
4	0	11	$\sqrt{5}$	Spherical
4	2	12	$\sqrt{10}$	2nd Astigmatism 0°
4	-2	13	$\sqrt{10}$	2nd Astigmatism 45°
4	4	14	$\sqrt{10}$	Tetrafoil 0°
4	-4	15	$\sqrt{10}$	Tetrafoil 22.5°

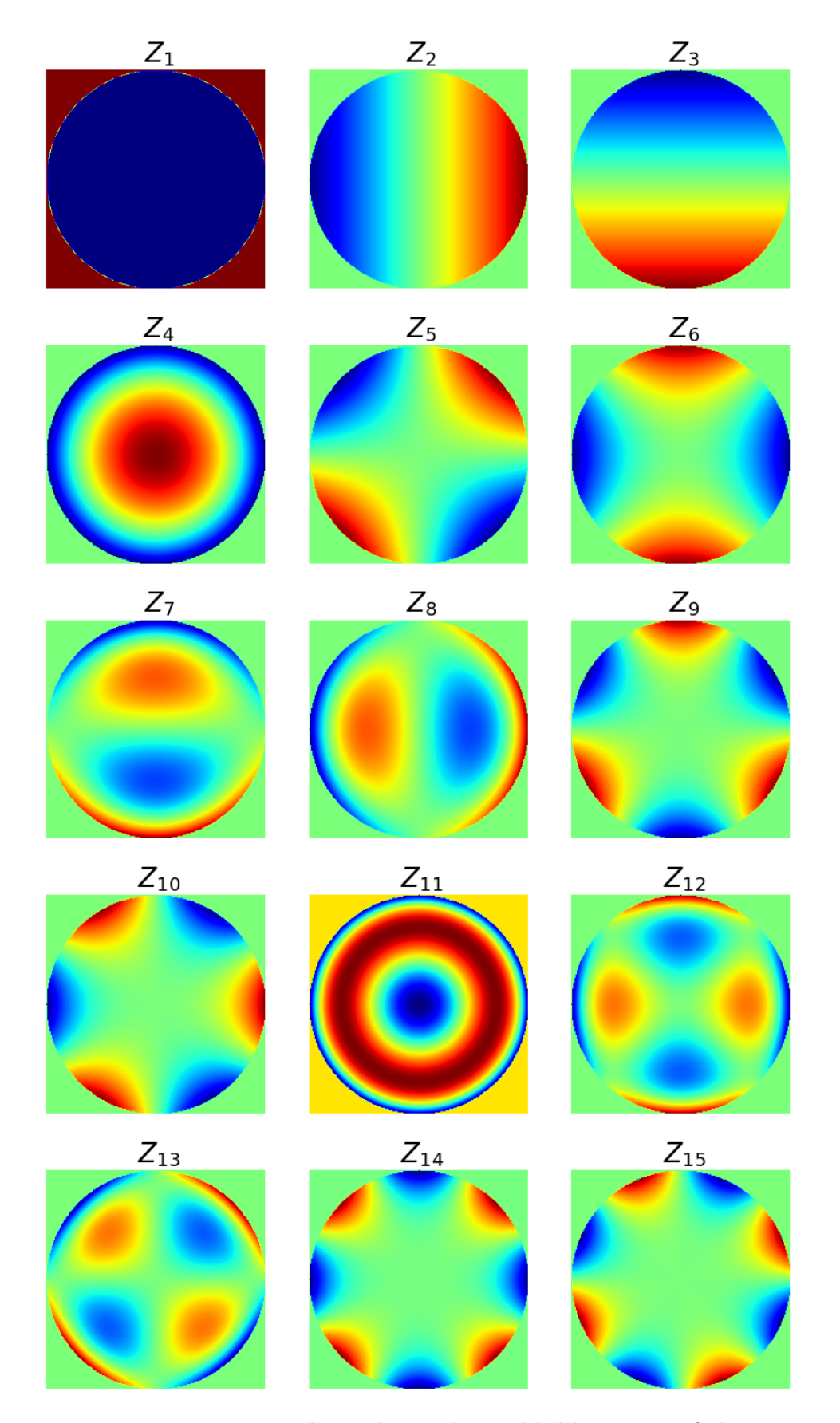


Figure 1.10: First 15 Zernike modes as phase added by 1 wave of aberration.

Chapter 2

Deformable Mirror (DM) Design and Control

As already anticipated there are many techniques to modulate the beam intensity, all based on spatially dividing the wavefront. The required strength of correction is applied with so called multi-channel correctors and is fundamental to compensate aberration modes higher than astigmatism. This application focuses on studying a Deformable Mirror (DM), because it permits to work with high-energy lasers in many applications.

2.1 Mechanical Structure and Properties of DMs

The evolution of correction devices clearly emerged prior to the inception of adaptive optics as an engineering discipline: devices used for real-time wavefront correction were reported by 1974, mainly to compensate for atmospheric turbulence. Although low-order aberrations, such as piston, tip and tilt, often requires having large-amplitude motion, high-order ones need high spatial frequencies and an actuator stroke of much less intensity. The development of high-energy lasers has pushed further the research for devices that could provide the correction of high-order modes while being less limited in temporal frequency response and able to survive high flux loads on the surfaces. In this case, DMs with multiple layer dielectric coatings with very high reflectivity must be used, in order to withstand the thermal loads and the stresses induced by the active deformation. Under these premises, a multi-actuator DM is a candidate for an all-purpose device and various technological solutions have been presented in literature.

Figure 2.1 summarizes the principal mechanical designs adopted. The main distinction is based on the type of surface: this latter can be composed by a regular geometric pattern of segments with tight gaps or can be a continuous plate to stretch using actuators. The earliest implementation of a DM has been the *segmented mirror*, a device made up of a number of closely spaced small mirrors with piston or

tilt correction capabilities. The non-continuous surface can be composed of square, hexagonal or circular segments. These are commonly operated in a piston-only mode, whereby each segment is confined to simple up-and-down motion, or in a piston / tip / tilt mode with three degrees of freedom, as illustrated in Figure 2.2.

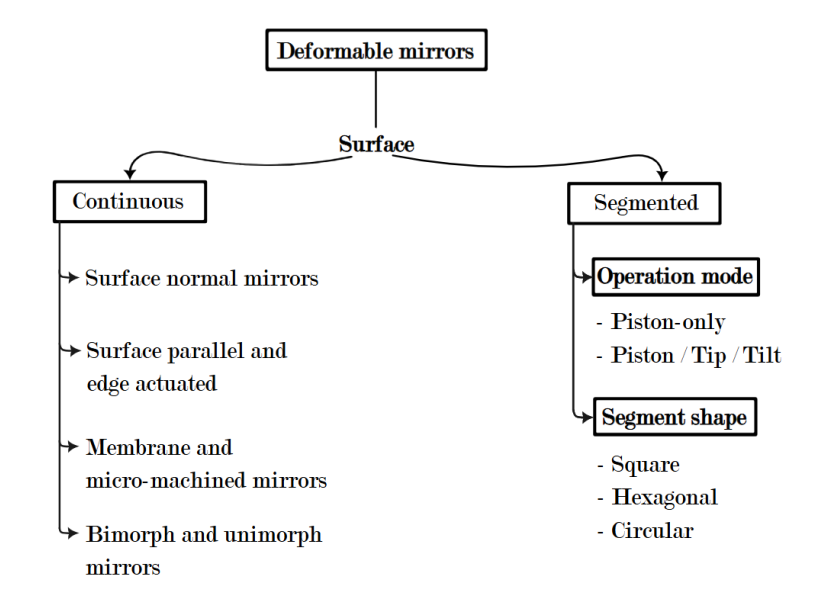


Figure 2.1: Mechanical characterization of DMs.

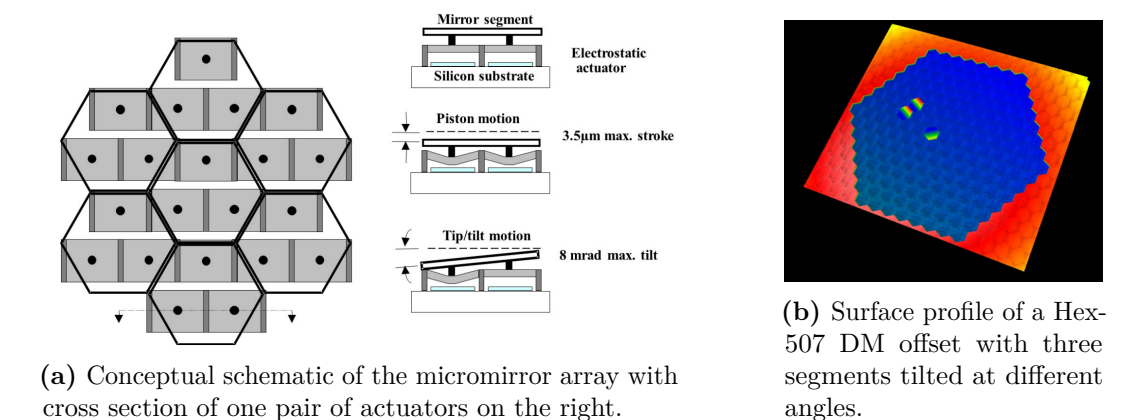


Figure 2.2: Example of Hex Tip-Tilt-Piston Deformable Mirror by [26].

A continuous surface requires the use of actuators to modify its shape: they can generally be characterized as either *constant force* or *constant displacement*, as shown in Figure 2.3.

Constant displacement actuators provide a displacement independent of the mass of the load, up to the blocking force limit. Ferroelectric devices are based on *electrostriction*, where the strain is proportional to the square of the electric field, as in lead-magnesium-niobate (PMN) components, or on the *converse piezoelectric effect*, where the strain is linearly dependent on the field, as in lead-zirconate-titanate (PZT)

Const. Displacement Ferroelectric Electrostriction Const. Force Lorentz Force Electrostatic Force Magnetostrictive

Figure 2.3: Actuators underlying mechanisms.

elements. The magnetostrictive actuators behave similarly to the electrostrictive ones, while the deformation is induced by the application of a magnetic field.

Constant force actuators on the other hand provide a constant force (acceleration): the most used are based on the *Lorentz force* principle, where the output is proportional to the magnetic field, or on the *electrostatic force*, where it is proportional to the square of the applied voltage.

From a control point-of-view, constant displacement devices can be easily used with position feedback controllers, while the constant force ones require a double integration.

The design choice between actuators depends on multiple phenomenons that need to be balanced such as ageing, creep, hysteresis, and maximum stroke obtained. For example, piezoelectric actuators can generally realize larger strains than electrostrictive devices and are suitable for fast feedback-based correction of low and high-order aberrations with large amplitude. However, they are more subject to ageing and hysteresis (from 7% up to 15% [22]). An optimized design must consider the particular field of application, in order to establish the maximum stroke needed, the response frequency, and the possibility of including other optical elements to compensate the effect of hysteresis or low-order aberrations, such as piston and tilt.

The DM surface can be deformed by actuators perpendicular to the membrane: Figure 2.4 shows devices based on (a) discrete position, (b) discrete force, and (c) bending moment actuators. Monolithic mirrors (d), instead, are produced as a single ceramic block with electrodes included in the design to obtain an higher actuator density and to avoid the limitations of manual work. The spring rates and damping within the mechanical structure of the generic DM can contribute to hysteresis, which influences the complexity of the control system and its closed-loop bandwidth. The mechanical characterization of the DM can also contribute to the description of the mirror dynamics as a reduced-order model [see 27, 28].

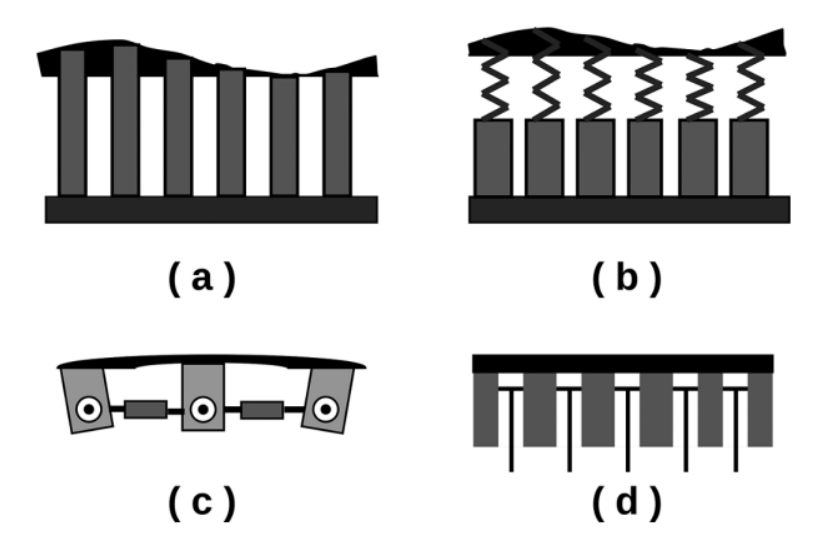


Figure 2.4: Continuous surface DMs: (a) discrete position actuators, (b) discrete force actuators, (c) bending moment actuators, (d) monolithic mirror [29].

Defocus and astigmatism are also corrected by moving the actuators in the same plane as the surface: bending moments and shears are induced applying voltage to piezoceramic wafers attached in parallel to the membrane or at its edge, as shown in Figure 2.5. This technical solution tend to have slow responses and broad influence functions due to deforming the entire structure.

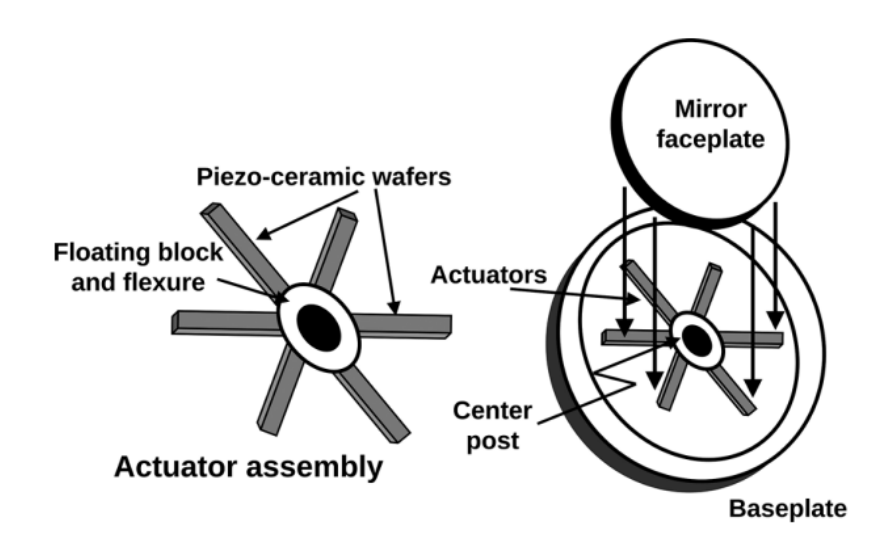


Figure 2.5: Structure of an edge actuated DM [29].

Another form of continuous surface mirror is the membrane mirror: the membrane is made of reflective materials or is fabricated by micro-machining of silicon or metal substrates, as in the Micro-machined Membrane Deformable Mirrors (MMDM). The bulk is mounted over a two-dimensional array of electrodes, as in Figure 2.6a. Any

potential applied between the membrane and the individual electrode, results in deformation of the membrane caused by electrostatic attraction. When no voltage differential is applied, the membrane remains flat. Nevertheless, combinations of voltages applied to different electrodes can form certain shapes on the surface. The local curvature of the surface, as reported in [29], can be expressed as

$$\nabla^2 z(x,y) = \frac{\partial^2 z(x,y)}{\partial x^2} + \frac{\partial^2 z(x,y)}{\partial y^2} = -\frac{P(x,y)}{T},$$
(2.1)

where T is the membrane tension (force/length) and P(x, y) is the electrostatic pressure (force/area) at position x, y.

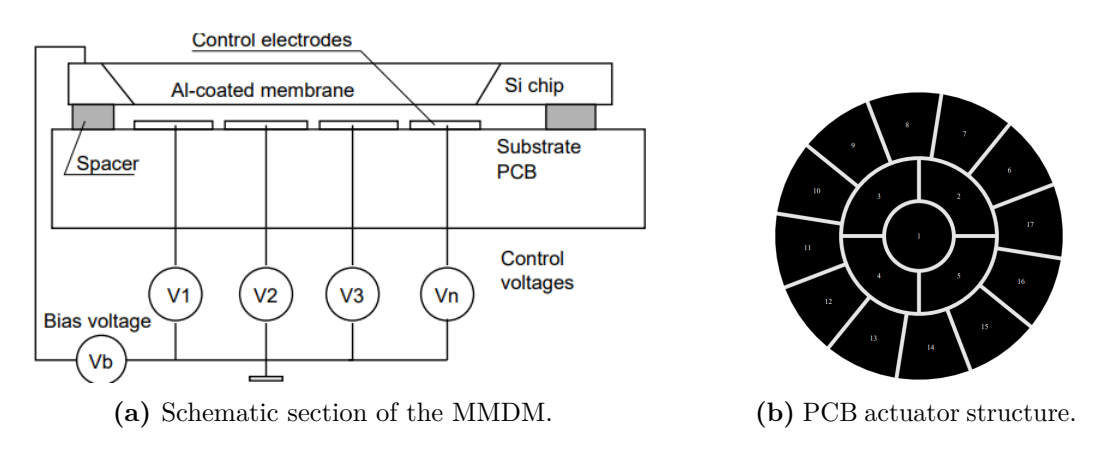


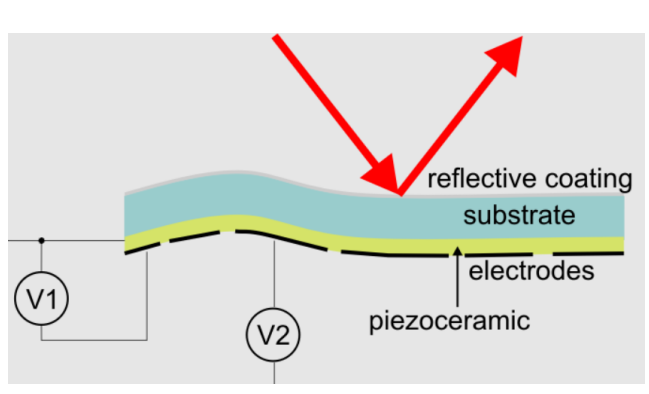
Figure 2.6: 17-channel MMDM from [30].

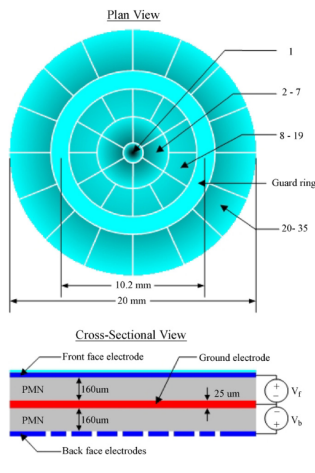
Similarly, bimorph and unimorph DMs have patterned electrodes, which modify the local curvature of the corrector proportionally to the applied voltage. As illustrated in Figure 2.7, the device is composed by a polished and coated thin layer, made of metal or glass, and glued to one piezoelectric disk for the unimorph DM or two for the bimorph DM. The PZT layer is polarized normal to the surface: when a voltage is applied to the electrodes, the orientation of the surface bending depends on the voltage polarity.

2.2 Compensation Techniques

In an AO system, phase is the fundamental physical variable that must be measured and represented. The dynamic systems used in research are characterised by a negative feedback control. Consequently, in addition to the hardware needed to implement the variations in phase, the loop must be closed with one or more sensors. in particular, wavefront sensing must have enough spatial resolution and speed to apply a real-time correction: both direct and indirect approach are usually employed.

In the first one, there is an explicit determination of the phase or OPD of the





(a) Schematic section of a unimorph DM [31].

(b) Layout of the AOptix DM studied in Horsley et al. [32].

Figure 2.7: Examples of unimorph and bimorph DMs.

wave; the reconstructed wavefront is then used as feedback to correct or modulate the phase. Due to the absence of phase sensitive detectors at optical wavelengths, wavefront sensing relies on devices that fundamentally measure intensity and must use optical designs, Fraunhofer diffraction patterns, or interferometric techniques to correlate the optical phase to its intensity distribution. As reported by [29], there is not an unique solution in the general case for phase retrieval from a single measurement of the PSF: to obtain the desired information multiple measurements of the pupil plane intensity and the image plane (Fraunhofer diffraction) intensity are required. Most researchers resort to iterative techniques, such as phase diversity [33], the maximum-likelihood algorithm [34], the Gerchberg-Saxton algorithm [35], and curvature sensing [36]. The large number of iterations required to generate a wavefront solution may result as a great limitation to real-time measurement and correction. Alternatively, the tailoring of the WFE can be posed as an optimization problem of an object function, which exploits the specific system characteristics (f.e. the type of the sensor data or the description of the desired intensity profile). This approach calls for improved and more sophisticated algorithms, that combine a global stepping search with local minimization at each step, such as heuristic and meta-heuristic methods. Some noticeable examples are genetic algorithms [37] and simulated annealing [38]. Many researchers have also resorted to deep reinforcement learning or self-learning, machine learning, and convolutional neural networks [see 39, 40, 41].

The indirect methods are mostly akin to trial and error: the intensity detected is coupled to the introduction of a phase delay in a closed-loop fashion to maximize the intensity distribution. This feedback system, shown in Figure 2.8, is the basis for the indirect techniques: the incoming beam has an unknown phase distribution δ_1 , which is modified adding a phase delay $\Delta \delta_1$, to obtain the desired intensity profile at

the detector. The term *hill climbing* [42] is often used for this method, due to the analogy with the act of climbing a hill to reach its summit. Some of the proposed methods are multi-dither AO systems, image sharpening, and full-field sensing (also called *digital adaptive optics*).

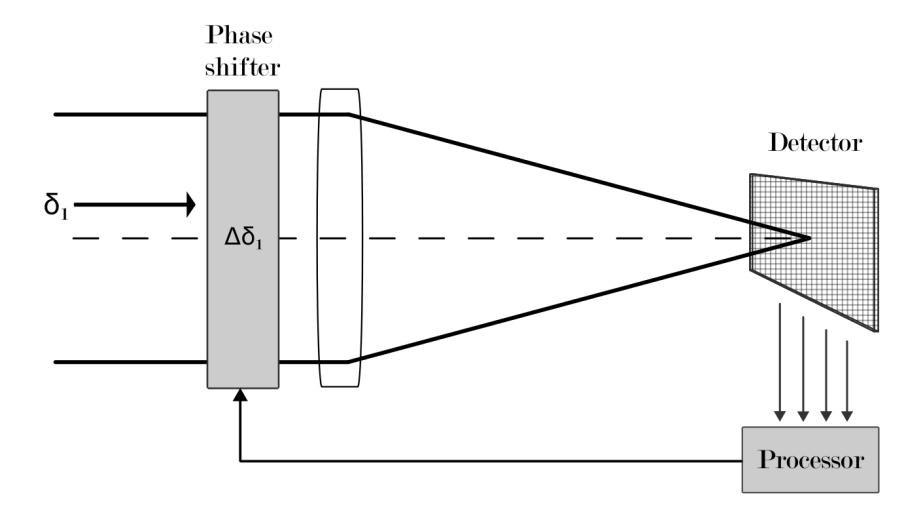


Figure 2.8: Indirect method of maximizing intensity.

Independently from the chosen approach, most conventional AO systems are implemented in a closed-loop fashion, as per the discrete block diagram in Figure 2.9. The data collected with the Wave-Front Sensor (WFS), along with the noise N(z), are processed through filtering algorithms H(z) and can be subject to phase reconstruction. After comparing the result to a reference R(z), the feedback error E(z) is obtained. This latter is fed to the controller, usually referred to as "driver", which activate the DM actuators G(z) through the voltage signal U(z). The latency block $\Lambda(z)$ accounts for the delayed response of the system, while the surface of the DM acts as the summing junction for the input beam and the added wavefront.

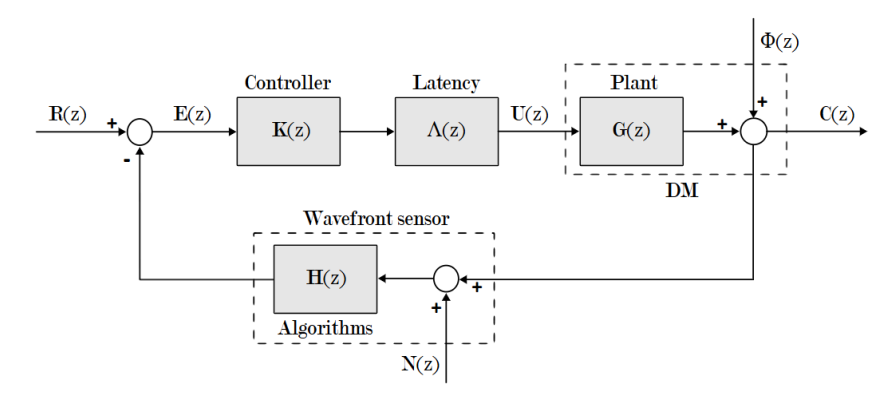


Figure 2.9: Example of negative feedback control scheme for AO.

The phase sensing, its reconstruction, and the DM commands can be zonal or modal. In zonal methods, the wavefront is spatially divided in N sub-apertures, in order to compute the individual WFE slope. Conversely, a modal description reduces the pupil phase to a linear combination of smooth polynomial functions (f.e. Power series, Zernike series, Hermite-Gaussian modes, Laguerre-Gaussian modes). Figure 2.10 shows possible paths to implement the closed-loop in conventional AO. The design choice to use modal, zonal, or a combination of sensing schemes to measure the wavefront is usually a consequence of the specific application. Similarly, some systems can limit the flexibility in using a certain WFE representation or the possibility of conversion from one into another; however, both describes the same physical variable. The presence of multiple discrete actuators in most of the technical solutions leads to firstly implement direct-drive commands in a zonal sense, while a sub-sequential decomposition into modal terms is possible.

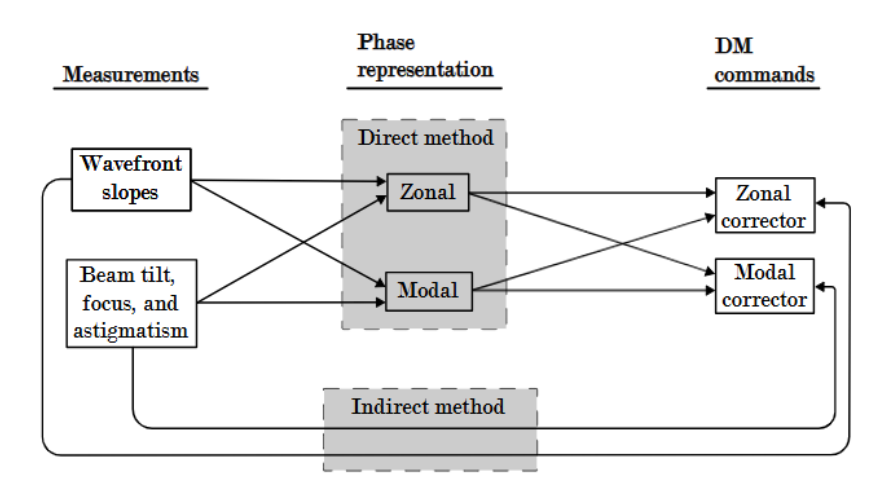


Figure 2.10: Possible paths of WFE control using AO.

2.2.1 Zonal compensation

The control of a DM in zonal sense requires the description of the shape of the actuated surface, also called the *influence function* of the mirror. It depends on the faceplate mechanical parameters, such as thickness, modulus of elasticity, and Poisson's ratio: these physical quantities are accounted in the finite element analysis or in the experimental analytic expressions proposed by researchers [see 29, p. 204]. The influence function of the DM correspond to the OPD added to the incoming beam to correct the spatially divided wavefront.

Considering the actuators as independent, the deflection of the surface S(x, y), within the boundaries of the mirror, is approximated by a linear combination of influence functions A_i as

$$S(x,y) = \sum_{i} A_{i}(x,y) \cdot v_{i} + S_{0}(x,y), \qquad (2.2)$$

where i denotes the actuator number, v_i the voltage applied, and S_0 the initial mirror shape. This formulation allows the description of a DM surface as a function of the applied voltages if the mathematical model of the actuator and the membrane is known.

For example, as reported by [22], the MMDM in Figure 2.6a can be modelled as a thin membrane of uniform thickness, stretched by a uniform surface tension T[N/m]. The distance d between the actuators grid and the membrane is considered much larger than the maximum deformation, so that the electrostatic pressure P does not depend on the membrane deflection. The resulting surface is described by the Poisson equation:

$$\Delta S(x,y) = \frac{P}{T},\tag{2.3}$$

where Δ is the Laplace operator and the electrostatic pressure P is given by:

$$P = \frac{\epsilon \ \epsilon_0 \ V(x, y)^2}{d(x, y)^2}.$$
 (2.4)

The solution to Equation 2.3 requires a set of boundary conditions and a finite difference numerical model for arbitrary geometries and pressure distributions.

Similarly, a simple mechanical model for a continuous faceplate DM (Figure 2.4) is derived from the small-deflection thin-plate one. The surface deflection S(x,y) is related to the actuators load acting on the plate P(x,y) and the cylindrical stiffness D, as:

$$\Delta \Delta S(x,y) = \frac{P(x,y)}{D},\tag{2.5}$$

In this case, D is given by:

$$D = \frac{Eh^3}{12(1-\nu)},\tag{2.6}$$

where E is the Young's modulus, h the thickness of the substrate, and ν the Poisson ratio.

2.2.2 Modal compensation

A system of modal correctors, such as tilt mirrors and focusing optics, or a DM designed to convert modal commands in zonal signals may be driven with knowledge of the correcting wavefront as a continuous phase map. This latter may be decomposed in the selected polynomial base Ψ , as:

$$\phi(x,y) = \sum_{j=1}^{n} c_{j} \Psi_{j}(x,y), \qquad (2.7)$$

The modes of the wavefront for the corrector can be determined by inverting the linear set of equation $\Phi = \Psi c$: only if the base is orthogonal, the matrix is diagonal and the inversion is simple. Decomposing the phase in Seidel aberrations or Zernike modes will require more computational effort, resulting in a rough approximation of the desired shape. An example of fitting for the aberration mix reported in Table 2.1 has been obtained through MrFit [43], a MS Windows program by OKO Technologies [44]. It calculates the voltages to be applied to the actuators, to achieve the best possible compensation with the selected mirror.

Table 2.1: Test aberration for MrFit.

$Z_{ m j}$	OPD [m]
Z_7	1×10^{-6}
Z_8	1×10^{-6}
Z_{10}	-1×10^{-6}
Z_{11}	1×10^{-6}
Z_{12}	-1×10^{-6}
Z_{13}	1×10^{-6}
Z_{14}	1×10^{-6}

Figure 2.11 shows the best fit for the reference wavefront using a MMDM with 37 active actuators and an illuminated aperture of 8 mm, obtaining a RMS error of 4.928×10^{-7} m. The test aberration has also been simulated on a membrane mirror with the same parameters, resulting in a RMS error of 1.598×10^{-7} m, as reported in Figure 2.12.

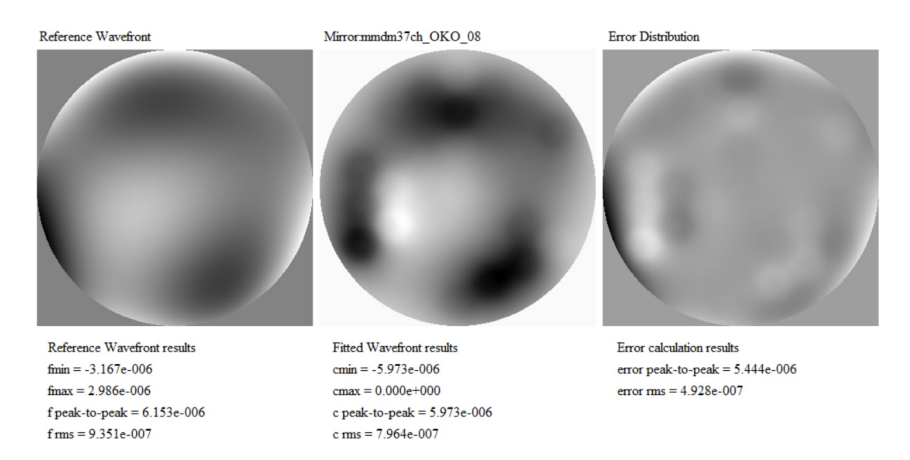


Figure 2.11: Correcting wavefront fitting with an OKO MMDM.

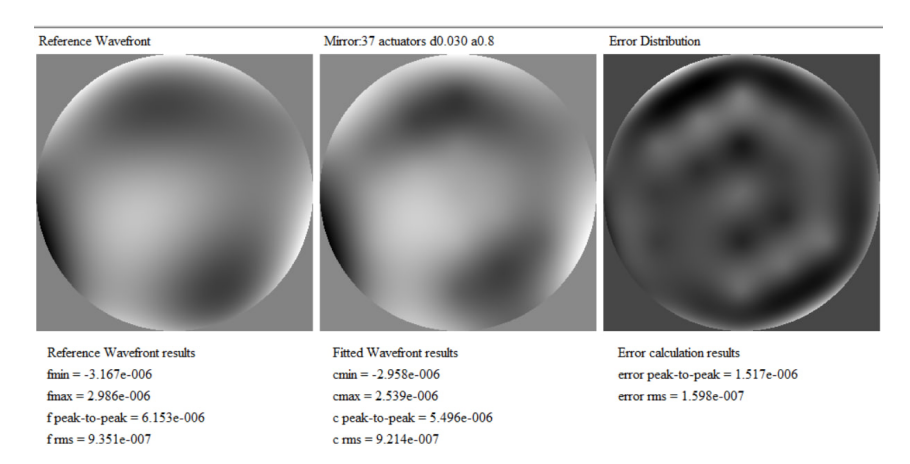


Figure 2.12: Correcting wavefront fitting with an OKO membrane mirror.

2.3 Selected DM Hardware

The AO hardware chosen for the experimental validation is the Dynamic Optics [45] piezoelectric bimorph deformable mirror DM3217. The faceplate in BK7 glass has a dielectric coating optimized at 1,030 nm to guarantee high damage threshold and high reflectivity. It is actuated with a pattern of 32 actuators (Figure 2.13b).

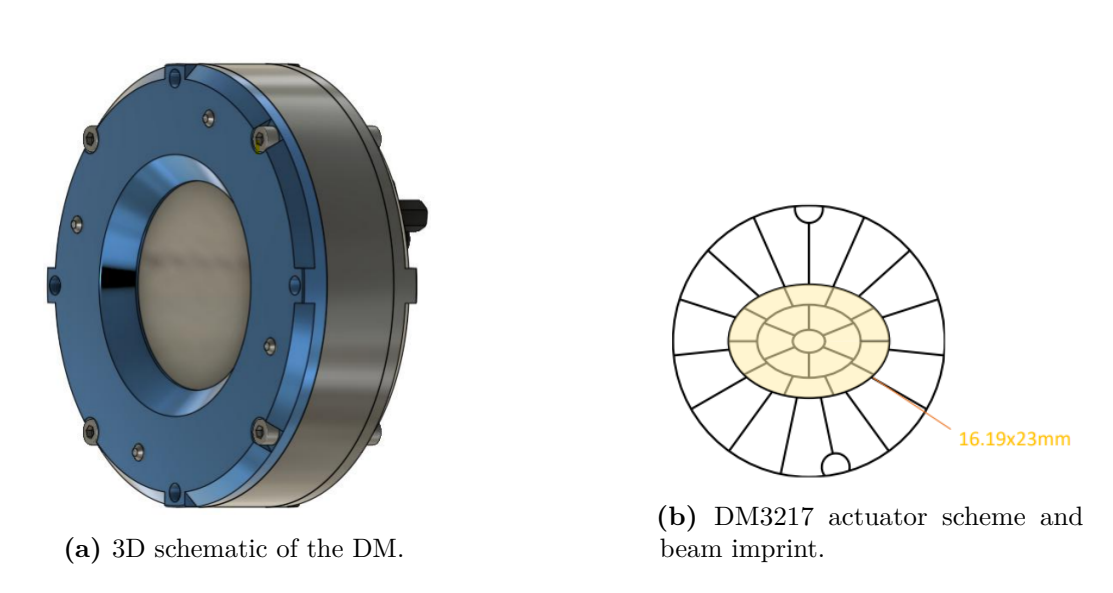
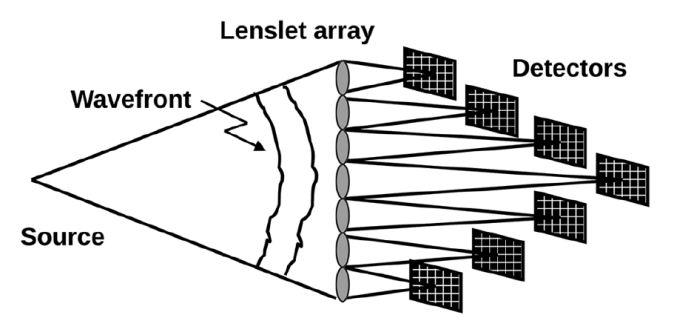


Figure 2.13: DM3217 piezoelectric bimorph deformable mirror from [45].

This double-layer bimorph allows for decoupling of defocus correction from higherorder wavefront correction, corresponding to a larger stroke for the defocus and better correction of low-order aberrations by offloading the stroke capability for other purposes. Improvements on the basic design include the addition of a second piezoelectric sheet bonded to the first with reverse polarization. When a voltage is applied to this configuration, the thickness does not increase, since one plate is contracting while the other is expanding. The opposing expansion—contraction results in the entire plate bending like a bimetallic strip with deformation occurring at the top and bottom surfaces. This device is ideal for for the correction of optical aberrations for many applications: high power lasers, ophthalmic imaging, microscopy and optical communications.

The negative feedback loop is closed inserting a Shack-Hartmann Wavefront Sensor (SHWS). In this device the wavefront is divided by a mask constituted by an array of gratings or an array of transmissive lenses, as in Figure 2.14a. Each of the beams in the sub-apertures is focused onto a detector. The modern Shack-Hartmann sensor is composed of an array of lenses for wavefront division and typically a CCD array with multiple pixels used for spot position (wavefront tilt) determination. Under most seeing conditions [see 29, p. 151], the SHWS performs better because of lower noise, while having a worse sensitivity than pyramid sensors. For the purpose of this thesis, the DM has been installed together with the sensor supplied by Dynamics Optics, a WS0150. This device, shown in Figure 2.14b, has a pixel size of 5.86 µm and a Clear Aperture (CA) of 13.4 mm.



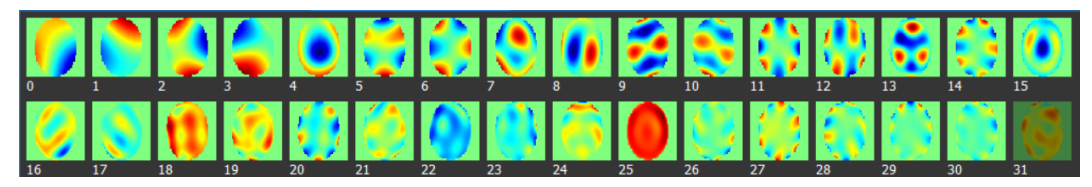


- (a) Shack–Hartmann wavefront sensing technique by [29].
- (b) Wavefront sensor chosen for implementation.

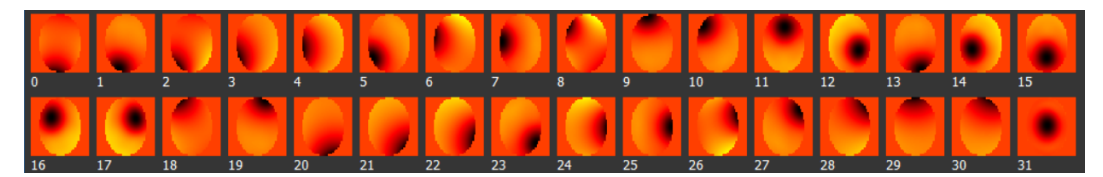
Figure 2.14: Shack-Hartmann wavefront sensor supplied by [45].

The DM, on the other hand, has a CA of 17 mm and can be installed at any angle of incidence (AoI). For example, the producer calibration test has been conducted at $AoI = 0^{\circ}$, resulting in the Zernike modes and corresponding influence functions in Figure 2.15.

During the experimental implementation, the DM has been positioned at a 45° AoI, using the provided brass alignment mask shown in Figure 2.16: the exiting beam is expected to have a diameter of 12 mm, when the major axis of the incoming elliptical footprint is aligned with the white markings on the mirror front.



(a) Reconstruction of Zernike modes with a DM3217.



(b) Influence functions of the corresponding Zernike terms.

Figure 2.15: Results of the DM3217 calibration at $AoI = 0^{\circ}$.

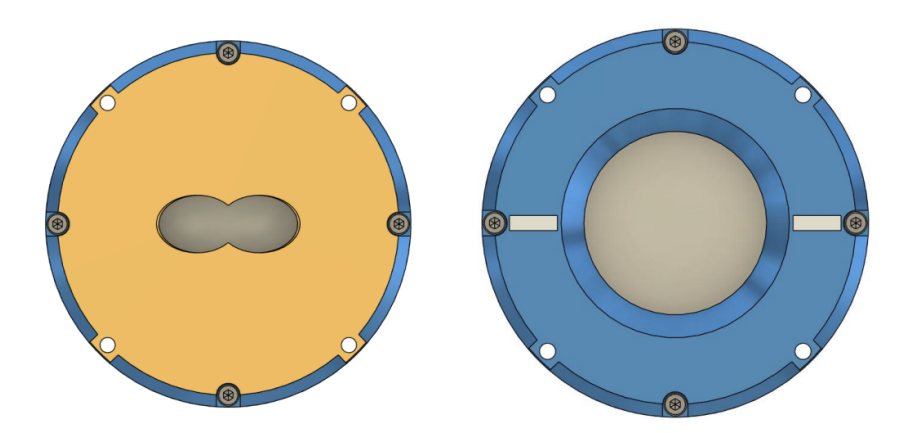


Figure 2.16: Brass alignment mask for correct centering at $AoI = 45^{\circ}$.

Chapter 3

Optical System Simulation

The correct design of an adaptive optics system also requires the correct choice of the optics surrounding the deformable mirror. This is because the insertion of a DM efficiently modulate the phase only if the device active diameter is comparable to the incoming beam e^{-2} diameter. For beam shaping applications, the AO elements usually have a limited number of actuators and small clear aperture (less than 20 mm). However, this characteristic dimension has a greater order of magnitude than the core of a commercial optic fiber. For example, Single-Mode Fibers (SMF), used for optical communications, sensing, and high quality lasers, have a 1.5 μm to 10 μm core. Multi-Mode Fibers (MMF), instead, have a core diameter of 25 µm, 200 µm and 600 µm: they are usually applied to short distance communications, imaging, illumination, and high power laser beams. For this reason, it has been decided to position the deformable mirror between a collimating lens and a focusing lens. At the same time, as previously described, the adaptive optics systems introduced in this thesis work with modes of aberrations, but the end user is typically not an optical engineer and, as such, needs to receive a set of Zernike coefficient values to obtain the desired shape. For this reason, an initial simulation programme was created in Python, then transferred to Zemax to take into account the phase effects caused by real optics compared to ideal optics.

3.1 Optical Chain Design

In order to obtain a collimated beam compatible with the chosen DM, a single collimating lens or a beam expander must be inserted between the fiber and the device. Both the solutions have been designed at wavelength $\lambda=630\,\mathrm{nm}$ and optimized to reach a nominal collimated beam of $\varnothing12\,\mathrm{mm}$, limiting the total length. A single-mode fiber S630-HP from Thorlabs [46] is the output for the laser source, with a pure silica core of $\varnothing3.5\,\mathrm{\mu m}$ and a nominal Numerical Aperture (NA) of 0.12.

The lens group in Figure 3.1 can be used to collimate at $\emptyset 12.365 \,\mathrm{mm}$ for a total axial length of $120.07 \,\mathrm{mm}$. As reported in Table 3.1, it is composed by a collimator

and a Galilean beam expander. This configuration has a greater axial length than a single collimator; however, it can be further optimized to compensate the spherical aberration introduced by the real lenses. The magnification factor M of the beam expander depends on the focal length f_1 of the negative lens and on the positive lens one f_2 , as:

$$M = \frac{f_2}{|f_1|} = \frac{w_2}{w_1}. (3.1)$$

It also relates the waist of the output beam w_2 with the waist of the incoming collimated beam w_1 , which is can be expressed as a function of the collimator focal length f_{coll} and the waist at the fiber core w_0 by Equation 3.2.

$$w_1 = \frac{\lambda f_{\text{coll}}}{\pi w_0} \tag{3.2}$$

Fixing $w_0 = 1.75 \,\mu\text{m}$, $\lambda = 630 \,\text{nm}$, and nominally $w_2 = 6 \,\text{mm}$, the real components are chosen to achieve the desired collimated diameter with an error of $3.042 \,\%$.

Table 3.1: Lens data for the collimator and beam expander configuration.

Element	Component	Thickness [mm]	Material			
Free space	-	22.80	Air			
Collimator	LA4021-A[47]	10.47	Fused silica			
Free space	-	5.00	Air			
Galilean beam expander						
Negative lens	LC4888-A[48]	3.50	Fused silica			
Free space	-	75.30	Air			
Positive lens	LA4924-A[49]	3.00	Fused silica			

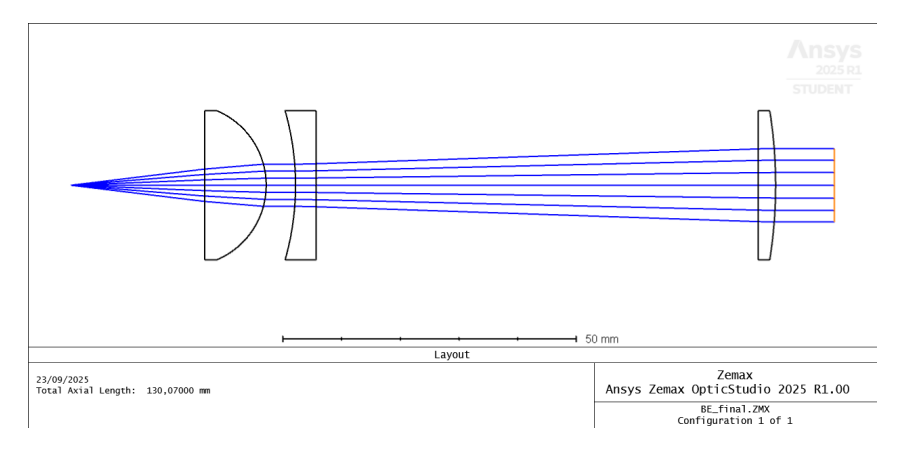


Figure 3.1: Lens group designed in Zemax OpticStudio for a more accurate beam expansion.

Conversely, a LA4148-A[50] plano-convex lens by Thorlabs has been chosen as

single collimating device: it has an Effective Focal Length (EFL) of $50.2\,\mathrm{mm}$ and, when inserted at the Back Focal Length $BFL=46.2\,\mathrm{mm}$, a collimated beam of $\varnothing 11.509\,\mathrm{mm}$ is obtained. This is the configuration adopted for the experimental implementation due to the reduced total axial length of $52.02\,\mathrm{mm}$, even if it gives a precision error of $4.092\,\%$ on the desired diameter.

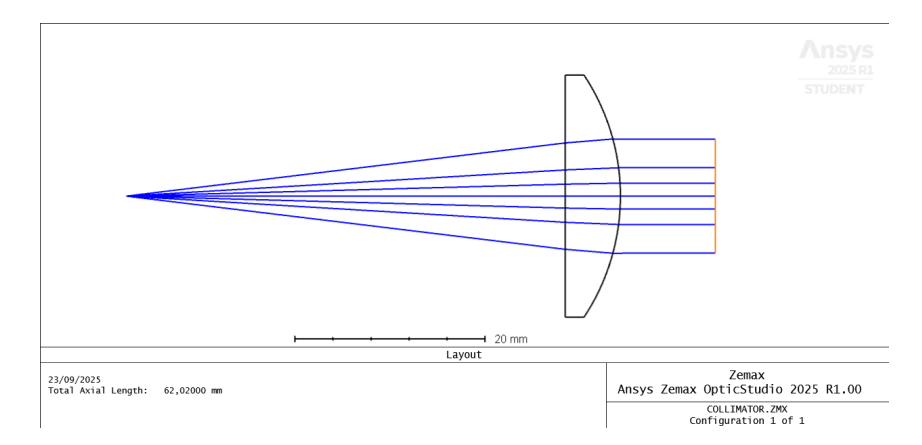


Figure 3.2: Single lens configuration for beam expansion.

Finally, a LA4663-A[51] converging lens by Thorlabs has been inserted after the DM to observe the beam at focus. The spot waist w_{focus} is related to the $EFL = 1,003.5 \,\text{mm}$, the wavelength λ , and the collimated beam waist w_{coll} by:

$$w_{\text{focus}} = \frac{\lambda \cdot EFL}{\pi w_{\text{coll}}},\tag{3.3}$$

resulting in a spot with $w_{\text{focus}} = 36.863 \,\mu\text{m}$ at $1,056.859 \,\text{mm}$ after the focusing lens. The final design of the optical chain to implement is reported in Table 3.2.

Element	Component	Thickness [mm]	Material
Free space	-	46.20	Air
Collimator	LA4148-A[50]	5.82	Fused silica
Free space	-	10.00	Air
Deformable mirror	DM3217[45]	2.00	BK7
Free space	-	10.00	Air
Focusing lens	LA4663-A[51]	2.18	Fused silica

Table 3.2: Final design of the implemented optical chain.

3.2 Python Simulation

The behaviour of the optical system in Table 3.2 is initially simulated in the *Beamspot Analyzer* software created by Dynamic Optics [45]. This program accepts the main geometrical parameters of the optical setup in Figure 3.3 and computes the PSF

of the system with the added phase mask applied on a grid plane according to the physical optics theory. The fiber cross section is then convoluted with the PSF to obtain the beamspot at focus and outside the focus plane.

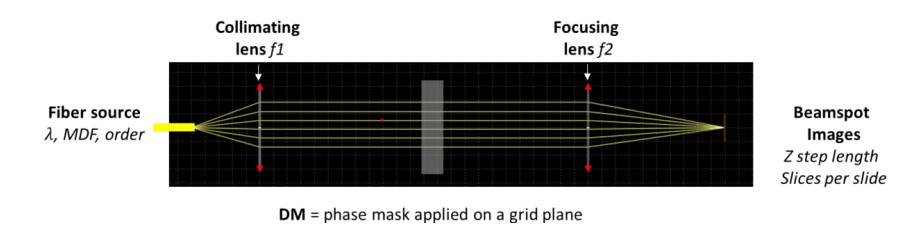


Figure 3.3: Sketch of the optical setup corresponding to the simulation process in *Beamspot Analyzer*.

Once the parameters are set, by clicking the *Simulate* button the software starts the computation and plots the results shown in Figure 3.4. The *Save File* button allows to save the simulated data in a numpy ".npz" file. Such file can be loaded within a Python session and used for further analysis on the slice images obtained at different z coordinates. The list of Zernike parameters is limited up to the first 15 modes, as in Table 1.2.

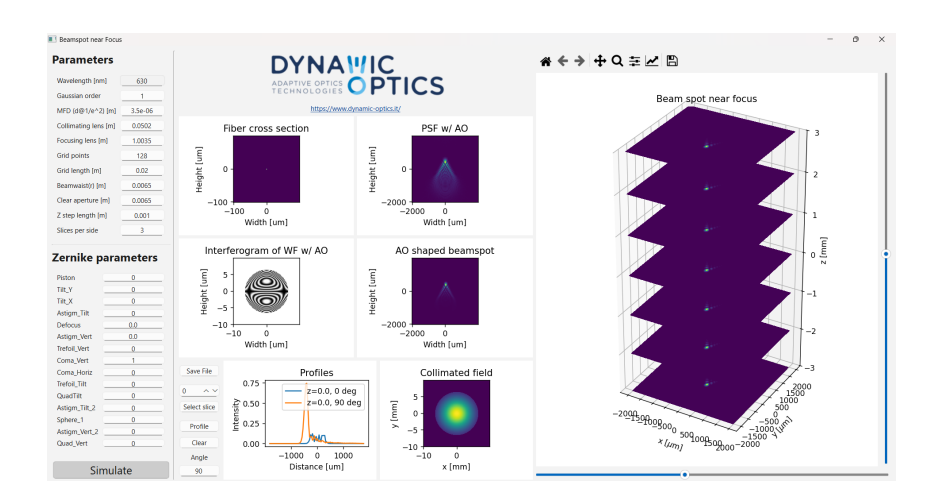


Figure 3.4: Main window of the software *Beamspot Analyzer* including the input column on the left, the focus-plane result plots in the central column and a 3D view of the beamspot around the image plane on the right.

In order to increase the Zernike terms included in the simulation and improve the results plotting, the part after collimation of the optical chain in Table 3.2 has been analysed using the LightPipes[52] package in Python. This toolbox is designed to model coherent optical devices when the diffraction is essential. The light beam is described as a large data structure, containing square two-dimensional arrays of complex amplitudes of the optical field. The package includes apertures, intensity filters, beam-splitters, ideal lenses, models of free space diffraction, and advanced tools for manipulating the phase and amplitude of light.

The Python code in Listing 3.1 simulates an ideal Gaussian beam collimated at $\emptyset 11.505\,\mathrm{mm}$ impacting on a DM, described by a Zernike phase mask, and being focused after 1,001.3 mm by an ideal lens with focal length $f=1,005.3\,\mathrm{mm}$. The input beam F is propagated to the phase mask as a pure Gaussian field using ABCD matrix theory(GForvard (F, z)), while a FFT (Fast Fourier Transform) algorithm(Forvard (F, z)) is required after aberration. The spherical coordinates method is introduced to model the diffraction into the focus of a lens with focal length shorter than the one used in the astronomic field. This technique uses the combination of a weak phase mask Lens(f1, F) and a strong geometrical coordinate transform LensFresnel(f2, z, F), reducing the number of grid points N and hence the execution time. The code returns the centroid of the focus intensity distribution and its width in the horizontal and vertical direction as $D4\sigma$ values, in order to better analyse the results.

Listing 3.1: Extract from the main code

```
## Beam data
          wavelength = 630*nm
          w0 = 1.75*um
          size = 13*mm
          f coll = 50.2*mm
         N = 2048
          ## Collimated radius
         w = (wavelength*f_coll)/(np.pi*w0)
10
11 ## Initialization of the Beam
12 F=Begin (size, wavelength, N)
F=GaussBeam (F, w)
          Iin=Intensity (0,F)
14
15
16 ##Zernike
          coef = [0.0]*40 #Modify with coefficients in waves
19 ## Propagation
_{20}|F = GForvard(F, 10*mm)
22 ## DM phase mask
        Dx, Dy = D4sigma(F)
23
        F = myzern(F, coef)
25
          phase=Phase(F,unwrap=False,units='rad')
26
27
         ## Last part of propagation
_{29}|F = Forvard(F, 10*mm)
30
        ## Spherical coordinates
|f| = 1003.5 *mm
33 f1=10*m
|f| = |f| + |f| + |f| + |f| = |f| + |f| 
|f_{foc}| = 1003.5*mm
```

```
frac=f/f1
newsize=frac*size*1e6
F=Lens(f1,0,0,F);
F=LensFresnel(f2,f,F);
F=Convert(F);

w_f = (wavelength*f_foc)/(np.pi*w)
sxf=w_f*2

## Intensity at focus
I = Intensity(0,F)
Xc,Yc, NXc, NYc = Centroid(F)
sx, sy = D4sigma(F)
```

The Zernike phase mask is introduced with the code in Listing 3.2, adding one aberration at time and slightly increasing the computation time. The radius of the aberrated aperture is fixed at 6.5 mm and the coefficients are given in multiples of the wavelength λ , in order to be compatible with the Dynamic Optics software and the Zemax simulation.

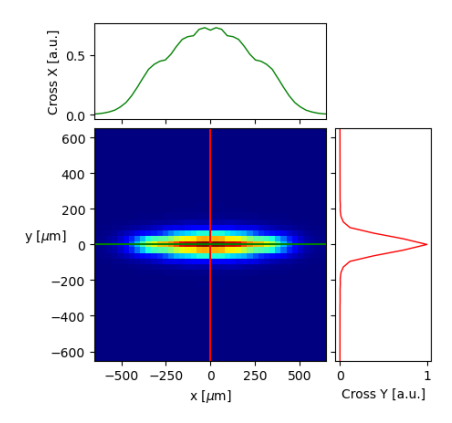
Listing 3.2: Phase mask function

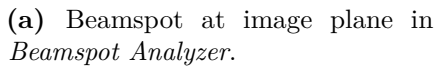
```
def myzern(F, coef):
    from LightPipes import D4sigma, noll_to_zern, Zernike, um, mm

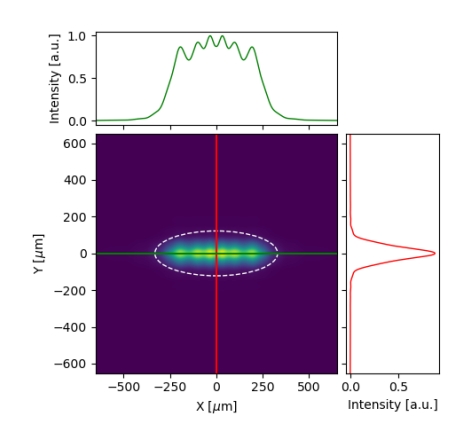
for Noll in range (1,len(coef)+1):
        (nz,mz)=noll_to_zern(Noll)
        F = Zernike(F, nz, mz, 6.5*mm, coef[Noll-1], units='lam')

return F
```

The Python simulation has been compared to Beamspot Analyzer, testing multiple combinations of aberration. Figure 3.5 represent the beam shaping effect of defocus $(Z_4 = 0.5 \text{ waves})$ and astigmatism at $0^{\circ}(Z_6 = 0.5 \text{ waves})$. In Figure 3.6 the same defocus is maintained, while trefoil along the Y axis $(Z_9 = -0.5 \text{ waves})$ is added. A mix of defocus $(Z_4 = 0.5 \text{ waves})$ and spherical aberration of the first order $(Z_{11} = 0.5 \text{ waves})$ has been considered in Figure 3.7. This results show the high compatibility of the two software, considering that they are both working in paraxial approximation, with ideal Gaussian beams, and ideal components.

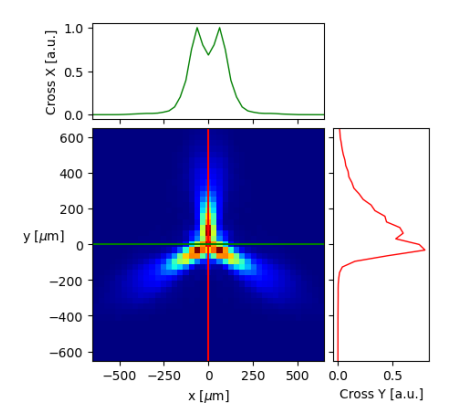




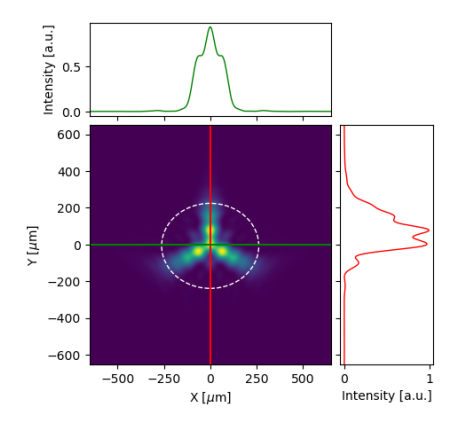


(b) Intensity plot at focus from the Python code.

Figure 3.5: Beam shaping with $Z_4 = 0.5$ waves and $Z_6 = 0.5$ waves.

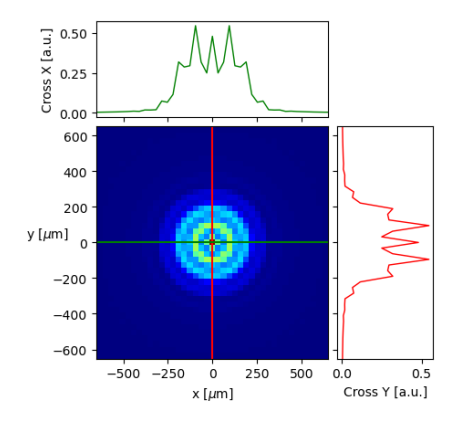


(a) Beamspot at image plane in Beamspot Analyzer.

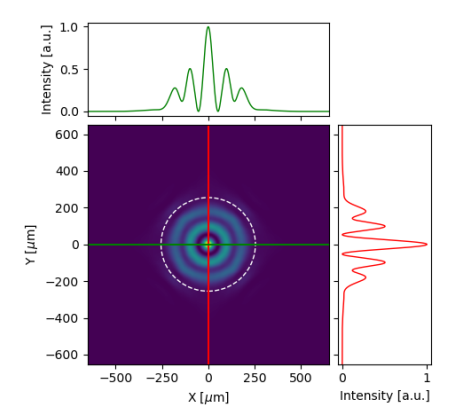


(b) Intensity plot at focus from the Python code.

Figure 3.6: Beam shaping with $Z_4 = 0.5$ waves and $Z_9 = -0.5$ waves.



(a) Beamspot at image plane in *Beamspot Analyzer*.



(b) Intensity plot at focus from the Python code.

Figure 3.7: Beam shaping with $Z_4 = 0.5$ waves and $Z_{11} = 0.5$ waves.

3.3 Zemax Implementation

The optical chain in Table 3.2 has been implemented in Ansys Zemax OpticStudio[53]. This latter is a software solution for designing components and sub-assemblies within complex, high-precision optical systems. Its key features are the ray tracing, the lens design tools, tolerance analysis, optimization, interoperability, multi-physics simulation and a user-friendly interface. For the purpose of this thesis, the optical system has been simulated in the sequential mode, where light rays are traced through a pre-defined sequence of surfaces, hitting each surface only once, while travelling from the object to the image plane. This modelling technique well describes imaging systems by sequential surfaces, while being computationally fast and extremely useful for the design, optimization, tolerancing, and analysis of such systems. The real lenses are inserted as ".zmx" files: in Figure 3.8 the collimating lens is highlighted in blue, while the focusing lens is reported in red.

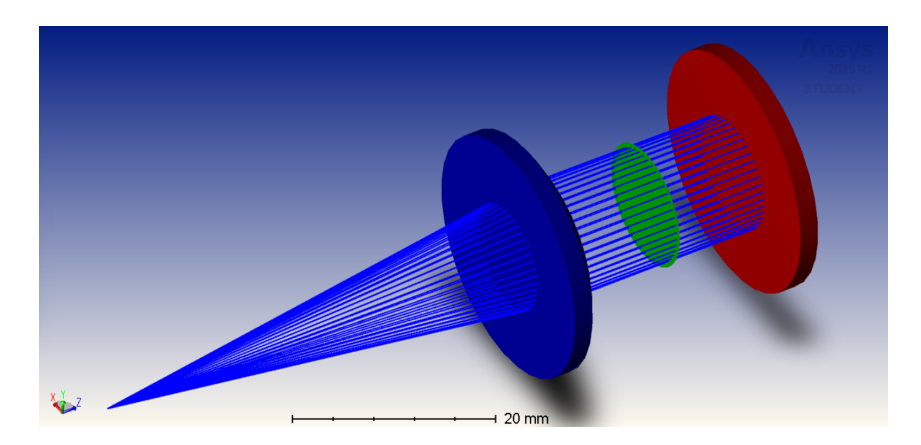


Figure 3.8: Zemax model of the optical chain reported in Table 3.2.

Conversely, the phase mask is simulated as a Zernike Standard phase surface and highlighted in green in Figure 3.8. This surface can model the system aberrations for which measured interferometer data is available. The additional phase terms deviate and add optical path to the rays as they cross the surface. According to Zemax manual, the phase is given by:

$$\Phi = M \sum_{i=1}^{N} 2\pi A_i Z_i(\rho, \varphi)$$
(3.4)

where N is the number of Zernike coefficients in the series, $A_{\rm i}$ is the coefficient of the $i^{\rm th}$ Zernike Standard polynomial, ρ is the normalized radial ray coordinate, φ is the angular ray coordinate, and M is the diffraction order. OpticStudio supports up to 231 terms and, as for the previous software, the coefficients $A_{\rm i}$ have units of waves. The normalization radius is, also, fixed at 6.5 mm.

The focus, computed at 1,056.859 mm after the focusing lens, is analysed through

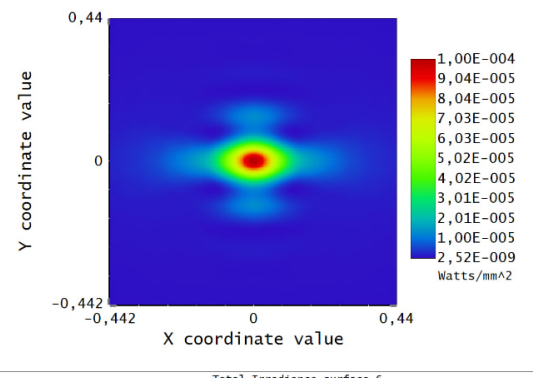
the features in the Image Quality Group and the Physical Optics Propagation (POP) tool. In particular, the wavefront error at each surface can be represented as a Wavefront Map over the pupil or as it would be seen on an interferometer.

To replicate the results obtained in section 3.2, the POP tool is used, modelling the optical system by propagating wavefronts. The beam is represented by an array of discretely sampled points, analogous to the discrete sampling using rays for a geometric optics analysis. The entire array is then propagated through the free space between optical surfaces. At each optical surface, a transfer function which transfers the beam from one side of the optical surface to the other is computed. Various data are obtained from this analysis: irradiance (beam power per area), phase, transfer function intensity, and transfer function phase can be displayed and saved. The same mixes of aberration have been tested in Zemax, correcting the coefficients sign according to the reference system of the pupil, as displayed in Figure 3.9.

To evaluate the impact of real components on the propagation of an ideal Gaussian beam in each test case, the wavefront error is represented as Wavefront Map both in Zemax and Python. The results are shown in Figure 3.10, Figure 3.11, and Figure 3.12. The WFE is expressed in number of waves over the normalized pupil at the DM surface, highlighting the presence of additional spherical aberration in the Zemax optical chain.

Moreover, a Zemax OpticStudio simulation already provides the description of multiple initial beams. While the non-sequential mode permits the insertion of a specific source in the lens data editor, the sequential mode allows the definition of a customizable initial beam in the POP panel. The modelled optical chain can be tested with an optionally truncated and decentered Hermite-Gaussian beam of arbitrary order, an Astigmatic Gaussian, a Top-Hat, a Multimode, and a user-defined beam described by a ".zbf" or a ".dll" file. For example, the Gaussian Angle, the Gaussian Size+Angle, and the Astigmatic Gaussian description are all suitable to input an elliptical beam with a possibly toroidal phase.

In conclusion, the Zemax model guarantees the best approximation of the real optical system and a flexible environment due to the programming features provided, such as the ZPL Macros and the Interactive Extensions. These latter allow connections from scripting environments(f.e. MATLAB, Python) to improve and boost the simulation performance.



Total Irradiance surface 6

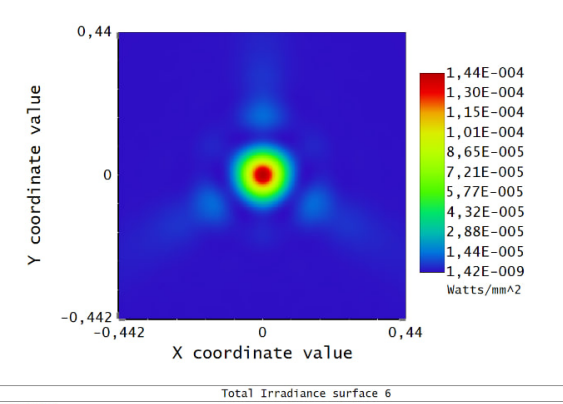
01/10/2025

Beam wavelength is 0,63000 um in the media with index 1,00000 at 0,0000 (deg)

Display X Width = 8,8406E-01, Y Height = 8,8406E-01 Millimeters
Peak Irradiance = 1,0046E-04 Watts/Millimeters
Pilot: Sizee 3,1647E-01, Watst= 3,8935E-02, Poss--6,1055E-01, Rayleigh= 7,5790E+00

Beam Width X = 1,66954E-00, Y = 1,68086E-00 Millimeters

(a) Beam shaping with $Z_4 = 0.5$ waves and $Z_6 = -0.5$ waves.



O1/10/2025

Beam wavelength is 0,63000 µm in the media with index 1,00000 at 0,0000 (deg)

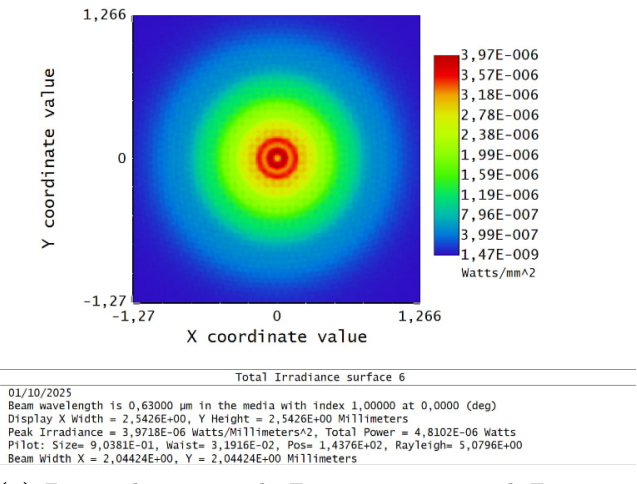
Display X Midth = 8,8406E-01, Y Height = 8,8406E-01 Millimeters

Peak Irradiance = 1,4412E-04 Watts/Millimeters/2, Total Power = 4,8102E-06 Watts

Pilot: 512e= 3,1647E-01, Waists = 3,8985E-02, Pose = 6,1055E-01, Rayleigh= 7,5790E+00

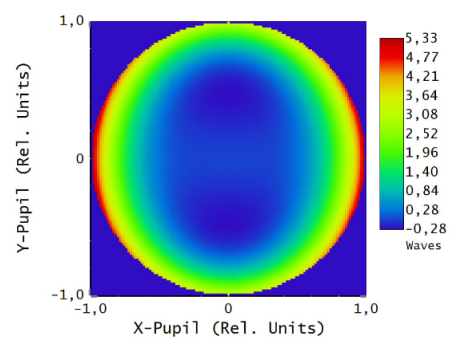
Beam Width X = 1,78618E+00, Y = 1,78548E+00 Millimeters

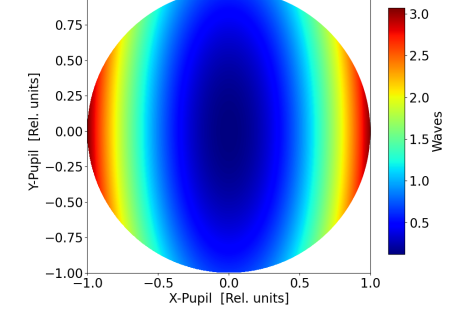
(b) Beam shaping with $Z_4 = 0.5$ waves and $Z_9 = -0.5$ waves.



(c) Beam shaping with $Z_4 = 0.5$ waves and $Z_{11} = 0.5$ waves

Figure 3.9: Total irradiance at focus from Zemax simulation.

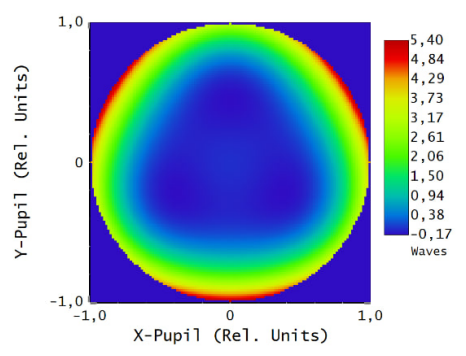


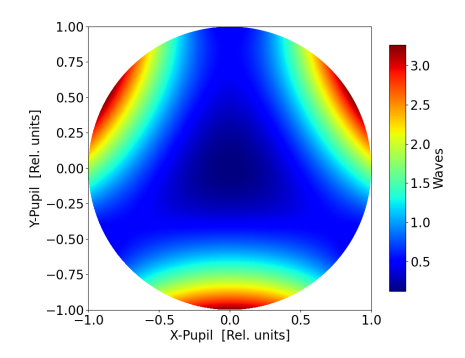


(a) Zemax Wavefront Map over the DM pupil.

(b) Python Wavefront Map over the DM pupil.

Figure 3.10: Wavefront error after $Z_4 = 0.5$ waves and $Z_6 = 0.5$ waves.

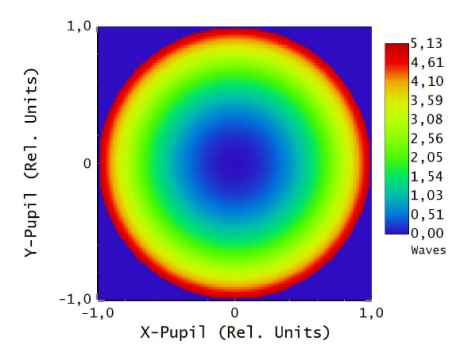




(a) Zemax Wavefront Map over the DM pupil.

(b) Python Wavefront Map over the DM pupil.

Figure 3.11: Wavefront error after $Z_4 = 0.5$ waves and $Z_9 = -0.5$ waves.



(a) Zemax Wavefront Map over the DM pupil.

(b) Python Wavefront Map over the DM pupil.

Figure 3.12: Wavefront error after $Z_4 = 0.5$ waves and $Z_{11} = 0.5$ waves.

Chapter 4

Experimental Implementation and Results

The chain designed in section 3.1 has been implemented in the laboratories of ALITE S.r.l. The mounted system includes the control driver, the Shack-Hartmann wavefront sensor, and a beam reducer to have a collimated beam with small diameter impacting on the sensor's lenslet array. The setup has been tested with a He-Ne source, emitting at wavelength $\lambda = 632.8\,\mathrm{nm}$ and with power $P = 10\,\mathrm{mW}$.

The negative feedback closed loop has been realised connecting the DM's driver and the SHWS to a PC, in order to configure the sensor's driver and interface both the devices with the software *PhotonLoop*. This latter is a high performance wavefront measurement and correction software, that interfaces to the Shack-Hartmann wavefront sensor and the deformable mirror. All the operations are aided with a friendly Graphical User Interface (GUI), facilitating access to the toolboxes needed for setup, calibration, control, and data collection. PhotonLoop can work up to 1 kHz and offers the possibility of data logging and remote control with TCP-IP. After calibration of the connected devices, the actuators voltage can be modified for the singular actuator or inserting the desired number of waves $N_{\rm w}$ for each aberration mode. If the objective of the test is the total compensation for aberrations, it is possible to choose the control law within the compensator settings widget, along with its parameters and additional robustness settings. These robustness parameters can help avoiding unexpected behaviours from the AO closed loop operations, such as to shut down the loop when the controller is self-oscillating or the sensor image is partially covered.

Conversely, an external and independent optimization process on the Zernike coefficients is needed to obtain the intensity profiles in Table 1.1 and implement a real dynamic beam shaping setup. This thesis doesn't investigate or apply any optimization algorithm, but is limited to the analysis of the characteristics of an AO system and a review of its feasibility. Comprehensive results on the beam shaping capabilities of this system have not yet been obtained due to lack of time. They may

therefore be one of the future developments on this topic, as well as the study of an optimization process.

4.1 Laboratory Optical Setup

The optical system schematized in Figure 4.1 has been replicated in laboratory, as shown in Figure 4.2.

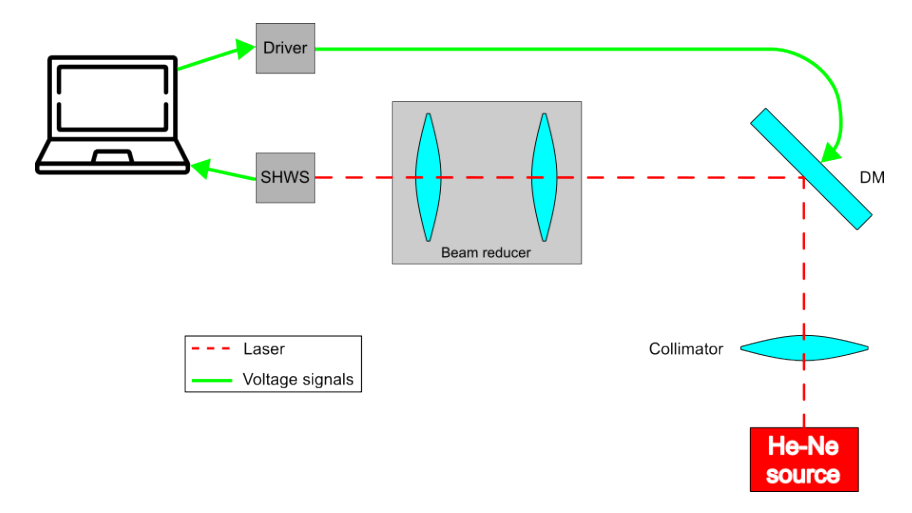


Figure 4.1: Scheme of the laboratory optical setup.

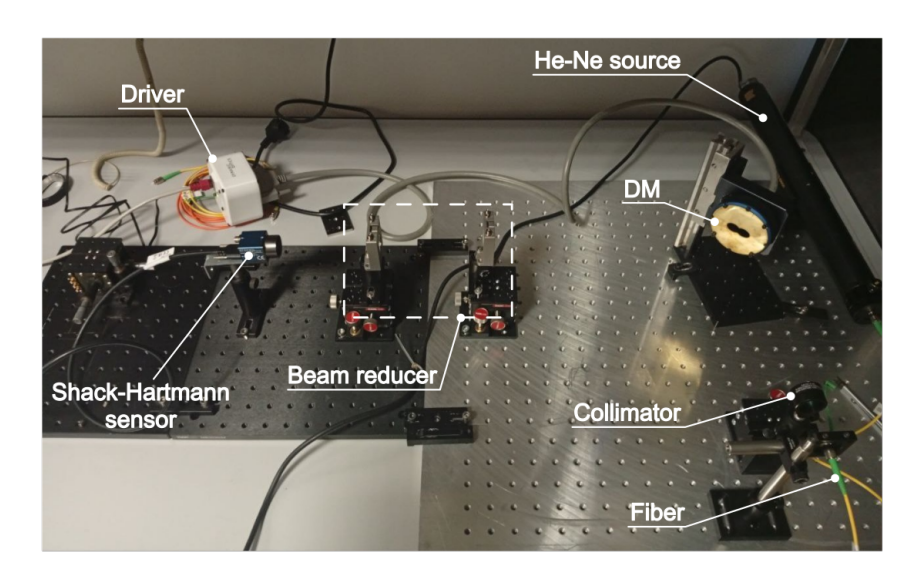


Figure 4.2: Laboratory setup for the DM testing.

The setup includes the components in Table 4.1.

Table 4.1: Components of the laboratory setup.

Component	Code	Manufacturer
Fiber	S630-HP	Thorlabs
Collimator	LA4148-A	Thorlabs
DM	DM3217	Dynamic Optics
Beam reducer		Thorlabs
SHWS	WS0150	Dynamic Optics
32 channels DM driver	PZT Multi	Dynamic Optics

4.2 Results

The experimental validation of the mounted setup in Figure 4.2 has not been completed. It was possible to align all the optical components and perform a calibration of the closed loop, as in Figure 4.3. The calibration reveals a strong aberrated beam and defects in the optical alignment. A proper test of the DM capabilities is still to schedule. Future modifications to the setup will include the addition of a beam splitter and a focusing lens to verify spot deformation at focus. Further possible improvements include the use of supports to correct angle defects in the positioning of the SHWS and the use of a single breadboard on which to mount the setup.

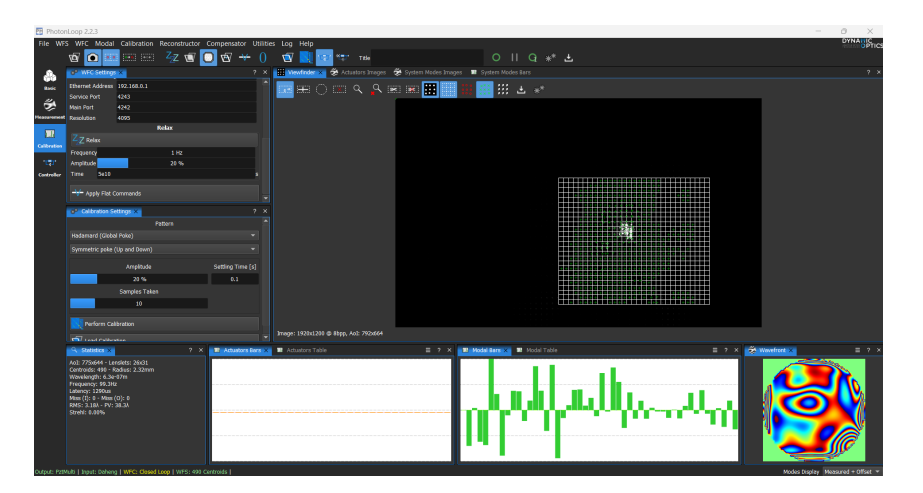


Figure 4.3: PhotonLoop window of a calibration process.

Chapter 5

Conclusions and Future Work

This Thesis addresses the feasibility of dynamic beam shaping through Adaptive Optics, to introduce a new process parameter in advanced industrial material manufacturing.

Firstly, the state of the art of adaptive optics in high-energy laser processing was explored in depth, with particular attention paid to Deformable Mirrors. A detailed analysis of their design was conducted in order to understand the potential of the DM3217 bimorph mirror produced by Dynamic Optics.

Secondly, a possible optical chain design was studied to include, simulate, and test the DM. The main challenges in this area concerned the compatibility of the results between the software provided by Dynamic Optics and the implementations created in Python and Zemax.

Finally, a laboratory setup based on the optical design was assembled in order to configure the wavefront measurement and correction software supplied with the mirror and to validate the simulations.

The simulations results demonstrate that the introduction of a DM enables significant enhancements in beam shaping flexibility, allowing quick adjustments of beam profiles, tailored to specific industrial processing needs. A proper test of the DM capabilities is still to schedule due to delays in sourcing components for the optical chain and in the configuration of the PhotonLoop software. However, this design is a starting point for the development of smarter laser manufacturing systems capable of higher precision, reduced processing times, and improved material properties.

In conclusion, the designed dynamic beam shaping system represents an intriguing possibility in high-energy laser technology with significant implications for industrial material processing. By harnessing the potential of deformable mirrors within an optimized optical chain, this work aims to improve the efficiency and versatility of the optical chain, supporting the goals of Industry 4.0 and beyond.

Bibliography

- [1] R. N. Wilson, F. Franza, and L. Noethe. "Active optics I. A system for optimizing the optical quality and reducing the costs of large telescopes". In: *Journal of Modern Optics* 34 (4 1987). ISSN: 13623044. DOI: 10.1080/09500348714550501 (cit. on p. 1).
- [2] Vikram M. Radhakrishnan, Christoph U. Keller, and Niek J. Doelman. "Towards real-time contrast control for direct exoplanet imaging with adaptive optics". In: *Optics Communications* 574 (Jan. 2025), p. 131046. ISSN: 0030-4018. DOI: 10.1016/J.OPTCOM.2024.131046. URL: https://www.sciencedirect.com/science/article/pii/S0030401824007831 (cit. on p. 1).
- [3] Michael Balas, Vethushan Ramalingam, Bhadra Pandya, Ahmed Abdelaal, and Runjie Bill Shi. "Adaptive optics imaging in ophthalmology: Redefining vision research and clinical practice". In: *JFO Open Ophthalmology* 7 (Sept. 2024), p. 100116. ISSN: 2949-8899. DOI: 10.1016/J.JFOP.2024.100116. URL: https://www.sciencedirect.com/science/article/pii/S2949889924000400 (cit. on p. 1).
- [4] Peiyi Zhang et al. "Deep learning driven adaptive optics for single molecule localization microscopy". In: *Biophysical Journal* 122 (3 Feb. 2023), 430a. ISSN: 0006-3495. DOI: 10.1016/J.BPJ.2022.11.2328. URL: https://www.sciencedirect.com/science/article/pii/S0006349522032441 (cit. on p. 1).
- [5] Kazumori Chida, Juichi Noda, Kazumasa Takada, and Itaru Yokohama. "New measurement system for fault location in optical waveguide devices based on an interferometric technique". In: Applied Optics, Vol. 26, Issue 9, pp. 1603-1606 26 (9 May 1987), pp. 1603-1606. ISSN: 2155-3165. DOI: 10.1364/AO.26.001603. URL: https://opg.optica.org/viewmedia.cfm?uri=ao-26-9-1603&seq=0&html=true%20https://opg.optica.org/abstract.cfm?uri=ao-26-9-1603%20https://opg.optica.org/ao/abstract.cfm?uri=ao-26-9-1603 (cit. on p. 1).
- [6] Huiyun Wu, Zhenhai Sun, Zhisong Huang, Jinbao Chen, and Rui Xiao. "Beam propagation through an optical system with the two-adaptive-optics configuration and beam shaping". In: *Optics & Laser Technology* 47 (Apr. 2013), pp. 315–322. ISSN: 0030-3992. DOI: 10.1016/J.OPTLASTEC.2012.09.012.

- URL: https://www.sciencedirect.com/science/article/abs/pii/S0030399212004185 (cit. on p. 1).
- [7] Jiang Bi, Liukun Wu, Shide Li, Zhuoyun Yang, Xiangdong Jia, Mikhail Dmitrievich Starostenkov, and Guojiang Dong. "Beam shaping technology and its application in metal laser additive manufacturing: A review". In: Journal of Materials Research and Technology 26 (Sept. 2023), pp. 4606–4628. ISSN: 2238-7854. DOI: 10.1016/J.JMRT.2023.08.037. URL: https://www.sciencedirect.com/science/article/pii/S2238785423018495?via%3Dihub (cit. on pp. 1, 3).
- [8] Rui Wang et al. "Demonstration of horizontal free-space laser communication with the effect of the bandwidth of adaptive optics system". In: *Optics Communications* 431 (Jan. 2019), pp. 167–173. ISSN: 0030-4018. DOI: 10.1016/J.OPTCOM.2018.09.038. URL: https://www.sciencedirect.com/science/article/abs/pii/S0030401818308198 (cit. on p. 1).
- [9] D. L. Simms. "Of Optics and Opticists". In: Applied Optics, Vol. 13, Issue 5, pp. A14-A16 13 (5 May 1974), A14-A16. ISSN: 2155-3165. DOI: 10.1364/A0.13. 000A14. URL: https://opg.optica.org/viewmedia.cfm?uri=ao-13-5-A14& seq=0&html=true%20https://opg.optica.org/abstract.cfm?uri=ao-13-5-A14%20https://opg.optica.org/ao/abstract.cfm?uri=ao-13-5-A14 (cit. on p. 2).
- [10] Isaac. Newton and Duane H. D.. Roller. "Opticks: or, a treatise of the reflections, refractions, inflections, & colours of light". In: (2015), p. 406 (cit. on p. 2).
- [11] Jannik Lind, Christian Hagenlocher, Niklas Weckenmann, David Blazquez-Sanchez, Rudolf Weber, and Thomas Graf. "Adjustment of the geometries of the cutting front and the kerf by means of beam shaping to maximize the speed of laser cutting". In: International Journal of Advanced Manufacturing Technology 126 (3-4 May 2023), pp. 1527–1538. ISSN: 14333015. DOI: 10.1007/S00170-023-11215-5/FIGURES/14. URL: https://link.springer.com/article/10.1007/s00170-023-11215-5 (cit. on p. 3).
- [12] Lin Wang, Xiangdong Gao, and Fanrong Kong. "Keyhole dynamic status and spatter behavior during welding of stainless steel with adjustable-ring mode laser beam". In: *Journal of Manufacturing Processes* 74 (Feb. 2022), pp. 201–219. ISSN: 1526-6125. DOI: 10.1016/J.JMAPRO.2021.12.011. URL: https://www.sciencedirect.com/science/article/abs/pii/S1526612521008835? via%3Dihub (cit. on p. 3).
- [13] W. A. Ayoola, W. J. Suder, and S. W. Williams. "Effect of beam shape and spatial energy distribution on weld bead geometry in conduction welding". In: Optics & Laser Technology 117 (Sept. 2019), pp. 280–287. ISSN: 0030-3992. DOI: 10.1016/J.OPTLASTEC.2019.04.025. URL: https://www.sciencedirect.com/science/article/pii/S0030399218313938?via%3Dihub (cit. on p. 3).

- [14] Yongcui Mi, Satyapal Mahade, Fredrik Sikström, Isabelle Choquet, Shrikant Joshi, and Antonio Ancona. "Conduction mode laser welding with beam shaping using a deformable mirror". In: Optics & Laser Technology 148 (Apr. 2022), p. 107718. ISSN: 0030-3992. DOI: 10.1016/J.OPTLASTEC.2021.107718. URL: https://www.sciencedirect.com/science/article/pii/S0030399221008 069?via%3Dihub (cit. on p. 3).
- [15] Handika Sandra Dewi, Andreas Fischer, Joerg Volpp, Thomas Niendorf, and Alexander F.H. Kaplan. "Microstructure and mechanical properties of laser surface treated 44MnSiVS6 microalloyed steel". In: Optics & Laser Technology 127 (July 2020), p. 106139. ISSN: 0030-3992. DOI: 10.1016/J.OPTLASTEC.2020. 106139. URL: https://www.sciencedirect.com/science/article/abs/pii/S0030399219317396?via%3Dihub (cit. on p. 3).
- [16] Evangelos Papastathopoulos et al. "Advances in beam shaping of high-power CW lasers with BrightLine weld technology". In: 11994 (Mar. 2022), p. 1199402. ISSN: 1996756X. DOI: 10.1117/12.2607138. URL: https://www.spiedigitallibrary.org/conference-proceedings-of-spie/11994/1199402/Advances-in-beam-shaping-of-high-power-CW-lasers-with/10.1117/12.2607138.full%20https://www.spiedigitallibrary.org/conference-proceedings-of-spie/11994/1199402/Advances-in-beam-shaping-of-high-power-CW-lasers-with/10.1117/12.2607138.short (cit. on p. 3).
- [17] N. J. Goffin, R. L. Higginson, and J. R. Tyrer. "The use of holographic optical elements (HOE's) to investigate the use of a flat irradiance profile in the control of heat absorption in wire-fed laser cladding". In: *Journal of Materials Processing Technology* 220 (June 2015), pp. 191-201. ISSN: 0924-0136. DOI: 10.1016/J.JMATPROTEC.2015.01.023. URL: https://www.sciencedirect.com/science/article/abs/pii/S0924013615000254?via%3Dihub (cit. on p. 3).
- [18] Yuhan Gao, Zhiyong An, Jinsong Wang, Weixing Zhao, and Fang Song. "Automatic optimization design of Gaussian beam shaping system by using ZEMAX software". In: *Optik* 122 (24 Dec. 2011), pp. 2176–2180. ISSN: 0030-4026. DOI: 10.1016/J.IJLEO.2011.02.006. URL: https://www.sciencedirect.com/science/article/abs/pii/S0030402611000775?via%3Dihub (cit. on p. 4).
- [19] Fly's Eye Homogenizers. URL: https://www.thorlabs.com/newgrouppage9.cfm?objectgroup_id=15169 (cit. on p. 4).
- [20] "DOEs for beam shaping". In: (). URL: http://www.SintecOptronics.comht tp://www.sintec.sg (cit. on p. 5).
- [21] Telescope image: rays, wavefront and diffraction. URL: https://www.telescope-optics.net/wave.htm (cit. on p. 8).
- [22] Catalogue. URL: https://www.okotech.com/catalogue (cit. on pp. 8, 14, 20).
- [23] Piezoelectric Deformable Mirrors. URL: https://www.thorlabs.com/newgrouppage9.cfm?objectgroup_ID=5056 (cit. on p. 8).

- [24] Spatial Light Modulators. URL: https://www.thorlabs.com/newgrouppage9.cfm?objectgroup_id=10378 (cit. on p. 8).
- [25] Robert J. Noll. "ZERNIKE POLYNOMIALS AND ATMOSPHERIC TURBULENCE." In: J Opt Soc Am 66 (3 1976). ISSN: 0030-3941. DOI: 10.1364/JOSA. 66.000207 (cit. on pp. 9, 10).
- [26] Segmented Deformable Mirror Boston Micromachines Corp. URL: https://bostonmicromachines.com/products/deformable-mirrors/hex-deformable-mirrors/ (cit. on p. 13).
- [27] Aleksandar Haber and Michel Verhaegen. "Modeling and state-space identification of deformable mirrors". In: Optics Express, Vol. 28, Issue 4, pp. 4726-4740 28 (4 Feb. 2020), pp. 4726-4740. ISSN: 1094-4087. DOI: 10.1364/OE.382880. URL: https://opg.optica.org/viewmedia.cfm?uri=oe-28-4-4726&seq=0&html=true%20https://opg.optica.org/abstract.cfm?uri=oe-28-4-4726%20https://opg.optica.org/oe/abstract.cfm?uri=oe-28-4-4726 (cit. on p. 14).
- O Kazasidis. "Methods for controlling deformable mirrors with hysteresis". In: (2021). DOI: 10.4233/UUID:3647C9BB-97D1-442A-9D3E-49CD1C9E3BAF. URL: https://repository.tudelft.nl/record/uuid:3647c9bb-97d1-442a-9d3e-49cd1c9e3baf (cit. on p. 14).
- [29] Robert K. Tyson and Benjamin W. Frazier. Principles of Adaptive Optics. 2022.
 DOI: 10.1201/9781003140191 (cit. on pp. 15–17, 19, 23).
- [30] Oleg Soloviev. "Adaptive Optics Optical Microsystems Wavefront Sensors 17-channel micromachined deformable mirror with built-in tip-tilt stage: technical passport OKO Technologies, OKO Technologies is the trade name of Flexible Optical BV". In: (). URL: www.okotech.com (cit. on p. 16).
- [31] Del Mar Photonics Bimorph Mirrors. URL: http://www.dmphotonics.com/Adaptive_Optics/bimorph_mirrors.htm (cit. on p. 17).
- [32] David A. Horsley, Hyunkyu Park, Sophie P. Laut, and John S. Werner. "Characterization of a bimorph deformable mirror using stroboscopic phase-shifting interferometry". In: Sensors and Actuators A: Physical 134 (1 Feb. 2007), pp. 221–230. ISSN: 0924-4247. DOI: 10.1016/J.SNA.2006.04.052. URL: https://www.sciencedirect.com/science/article/abs/pii/S0924424706003281 (cit. on p. 17).
- [33] Robert A. Gonsalves. "Phase Retrieval And Diversity In Adaptive Optics". In: https://doi.org/10.1117/12.7972989 21 (5 Oct. 1982), pp. 829-832. ISSN: 0091-3286. DOI: 10.1117/12.7972989. URL: <a href="https://www.spiedigitallibrary.org/journals/optical-engineering/volume-21/issue-5/215829/Phase-Retrieval-And-Diversity-In-Adaptive-Optics/10.1117/12.7972989. full%20https://www.spiedigitallibrary.org/journals/optical-engineering/volume-21/issue-5/215829/Phase-Retrieval-And-Diversity-In-Adaptive-Optics/10.1117/12.7972989. short (cit. on p. 17).

- [34] K. Aditya Mohan, Jean Baptiste Forien, Venkatesh Sridhar, Jefferson Cuadra, and Dilworth Parkinson. "Maximum Likelihood Based Phase-Retrieval Using Fresnel Propagation Forward Models With Optional Constraints". In: *IEEE Transactions on Computational Imaging* 9 (2023), pp. 1111–1125. ISSN: 23339403. DOI: 10.1109/TCI.2023.3332007 (cit. on p. 17).
- [35] John C. Zingarelli and Stephen C. Cain. "Phase retrieval and Zernike decomposition using measured intensity data and the estimated electric field". In: Applied Optics, Vol. 52, Issue 31, pp. 7435-7444 52 (31 Nov. 2013), pp. 7435-7444. ISSN: 2155-3165. DOI: 10.1364/A0.52.007435. URL: https://opg.optica.org/viewmedia.cfm?uri=ao-52-31-7435&seq=0&html=true%20https://opg.optica.org/abstract.cfm?uri=ao-52-31-7435%20https://opg.optica.org/ao/abstract.cfm?uri=ao-52-31-7435 (cit. on p. 17).
- [36] Xuan Xie, Bocheng Wang, Bocheng Wang, Hairen Wang, and Hairen Wang. "Method of wavefront phase retrieval from wavefront curvature sensing using membrane modes". In: Applied Optics, Vol. 61, Issue 33, pp. 10043-10048 61 (33 Nov. 2022), pp. 10043-10048. ISSN: 2155-3165. DOI: 10.1364/A0.472772. URL: https://opg.optica.org/viewmedia.cfm?uri=ao-61-33-10043& seq=0&html=true%20https://opg.optica.org/abstract.cfm?uri=ao-61-33-10043%20https://opg.optica.org/ao/abstract.cfm?uri=ao-61-33-10043 (cit. on p. 17).
- [37] Hong Cheng, Zijing Hu, Jinyu Fang, al -, Wei Yin, Jinxin Zhong, Shijie Feng, Randy Lemons, and Sergio Carbajo. "Phase retrieval and reconstruction of coherent synthesis by genetic algorithm". In: Journal of Physics: Photonics 4 (2 Mar. 2022), p. 026001. ISSN: 2515-7647. DOI: 10.1088/2515-7647/AC4AFD. URL: https://iopscience.iop.org/article/10.1088/2515-7647/ac4afd%20https://iopscience.iop.org/article/10.1088/2515-7647/ac4afd/meta (cit. on p. 17).
- [38] F. J. Fuentes, R. Navarro, and M. Nieto-Vesperinas. "Performance of a simulated annealing algorithm for phase retrieval". In: JOSA A, Vol. 5, Issue 1, pp. 30-38 5 (1 Jan. 1988), pp. 30-38. ISSN: 1520-8532. DOI: 10.1364/JOSAA.5.000030. URL: https://opg.optica.org/viewmedia.cfm?uri=josaa-5-1-30&seq= 0&html=true%20https://opg.optica.org/josaa/abstract.cfm?uri=josaa-5-1-30 (cit. on p. 17).
- [39] Jonathan Dong, Lorenzo Valzania, Antoine Maillard, Thanh An Pham, Sylvain Gigan, and Michael Unser. "Phase Retrieval: From Computational Imaging to Machine Learning: A tutorial". In: *IEEE Signal Processing Magazine* 40 (1 Jan. 2023), pp. 45–57. ISSN: 15580792. DOI: 10.1109/MSP.2022.3219240 (cit. on p. 17).
- [40] Ying-Ju Chen et al. "Self-supervised neural network for phase retrieval in QDPC microscopy". In: Optics Express, Vol. 31, Issue 12, pp. 19897-19908 31

- (12 June 2023), pp. 19897-19908. ISSN: 1094-4087. DOI: 10.1364/0E.491496. URL: https://opg.optica.org/viewmedia.cfm?uri=oe-31-12-19897& seq=0&html=true%20https://opg.optica.org/abstract.cfm?uri=oe-31-12-19897%20https://opg.optica.org/oe/abstract.cfm?uri=oe-31-12-19897 (cit. on p. 17).
- [41] Daniele Orsuti, Cristian Antonelli, Senior Member, Alessandro Chiuso, Marco Santagiustina, Antonio Mecozzi, Andrea Galtarossa, and Luca Palmieri. "Deep Learning-Based Phase Retrieval Scheme for Minimum-Phase Signal Recovery". In: Journal of Lightwave Technology, Vol. 41, Issue 2, pp. 578-592 41 (2 Jan. 2023), pp. 578-592. DOI: 10.1109/JLT.2022.3219639. URL: https://opg.optica.org/abstract.cfm?uri=jlt-41-2-578%20https://opg.optica.org/jlt/abstract.cfm?uri=jlt-41-2-578 (cit. on p. 17).
- [42] Ying Liu, Jianqiang Ma, Baoqing Li, and Jiaru Chu. "Hill-climbing algorithm based on Zernike modes for wavefront sensorless adaptive optics". In: https://doi.org/10.1117/1.0E.52.1.016601 52 (1 Jan. 2013), p. 016601. ISSN: 0091-3286. DOI: 10.1117/1.0E.52.1.016601. URL: https://www.spiedigitallibrary.org/journals/optical-engineering/volume-52/issue-1/016601/Hill-climbing-algorithm-based-on-Zernike-modes-for-wavefront-sensorless/10.1117/1.0E.52.1.016601.full%20https://www.spiedigitallibrary.org/journals/optical-engineering/volume-52/issue-1/016601/Hill-climbing-algorithm-based-on-Zernike-modes-for-wavefront-sensorless/10.1117/1.0E.52.1.016601.short (cit. on p. 18).
- [43] MrFit: mirror simulation software | Software | Products. URL: https://www.okotech.com/mrfit (cit. on p. 21).
- [44] Welcome to Flexible Optical B.V.! URL: https://www.okotech.com/ (cit. on p. 21).
- [45] Adaptive Optics Technologies DYNAMIC OPTICS. URL: https://www.dynamic-optics.it/(cit. on pp. 22, 23, 27).
- [46] Thorlabs S630-HP Single Mode Optical Fiber, 630 860 nm, Ø125 μ m Cladding. URL: https://www.thorlabs.com/thorproduct.cfm?partnumber= S630-HP (cit. on p. 25).
- [47] Thorlabs LA4021-A f = 30 mm, $\emptyset1''$ UVFS Plano-Convex Lens, ARC: 350 700 nm. URL: https://www.thorlabs.com/thorproduct.cfm?partnumber= LA4021-A (cit. on p. 26).
- [48] Thorlabs LC4888-A \emptyset 1", f = -100 mm, UV Fused Silica Plano-Concave Lens, ARC: 350 700 nm. URL: https://www.thorlabs.com/thorproduct.cfm? partnumber=LC4888-A (cit. on p. 26).
- [49] Thorlabs LA4924-A f = 175 mm, Ø1" UVFS Plano-Convex Lens, ARC: 350 700 nm. URL: https://www.thorlabs.com/thorproduct.cfm?partnumber=LA4924-A (cit. on p. 26).

BIBLIOGRAPHY

- [50] Thorlabs LA4148-A f = 50 mm, $\emptyset1''$ UVFS Plano-Convex Lens, ARC: 350 700 nm. URL: https://www.thorlabs.com/thorproduct.cfm?partnumber= LA4148-A (cit. on pp. 26, 27).
- [51] Thorlabs LA4663-A f = 1000 mm, $\emptyset1''$ UVFS Plano-Convex Lens, ARC: 350 700 nm. URL: https://www.thorlabs.com/thorproduct.cfm?partnumber= LA4663-A (cit. on p. 27).
- [52] 1. Introduction. LightPipes for Python 2.1.5 documentation. URL: https://opticspy.github.io/lightpipes/introduction.html (cit. on p. 28).
- [53] Ansys Zemax OpticStudio / Optical Design and Analysis Software. URL: https://www.ansys.com/products/optics/ansys-zemax-opticstudio (cit. on p. 32).

Dedications

I would like to thank my primary supervisor, Prof. Guido Perrone, who guided me throughout this project with his insightful comments and suggestions. I wish to extend my special thanks to my supervisors Ing. Sabina Zaimovic and Ing. Valentina Serafini for teaching me how to survive Zemax and all their help with this thesis.

My heartfelt thanks to Ing. Gabriella Motta and the family of ALITE S.r.l. for the technical support and counselling and the continuous attempts on my diet.

I would like to express my sincere gratitude to my family for their unwavering love and comprehension. It couldn't have been the same without my sisters Vittoria, Anna and Domenica, who tolerate my yapping on the thesis and usually me. All my love to my parents, Carmela and Giuseppe, who have always believed that I'll probably design weapons for work one day ans also in me. I wish to acknowledge the psychological help offered by my dogs, Boby and Maia, who are always so needy and compulsively adorable.

To my boyfriend, Mario, who is a sweet potato and a radiator until proven otherwise. You sustained me through all of that sorrow and the truth of the matter is you never let me go.